Fuel 127 (2014) 186–201

Contents lists available at ScienceDirect

Fuel

journal homepage: www.elsevier.com/locate/fuel

CO_2-gasification of a lignite coal in the presence of an iron-based oxygen carrier for chemical-looping combustion

Marco A. Saucedo [a,*], Jin Yang. Lim [a], John S. Dennis [a], Stuart A. Scott [b]

[a] University of Cambridge, Department of Chemical Engineering and Biotechnology, New Museums Site, Pembroke Street, Cambridge CB2 3RA, United Kingdom
[b] University of Cambridge, Department of Engineering, Trumpington Street, Cambridge CB2 1PZ, United Kingdom

HIGHLIGHTS

- A lignite was found to be a promising type of solid fuel for chemical-looping.
- Intrinsic kinetics of gasification were described by the modified Ergun equation.
- Enhancement of the apparent rate of gasification of lignite when Fe_2O_3 was present.
- Mass transfer limitations within and surrounding the particle were modelled.
- Changes in the surface area and build-up of CO at the surface were considered.

ARTICLE INFO

Article history:
Received 15 April 2013
Received in revised form 3 July 2013
Accepted 16 July 2013
Available online 30 July 2013

Keywords:
Chemical looping combustion
Iron oxide
Gasification
Coal
CO_2 capture

ABSTRACT

Chemical-looping combustion (CLC) has the inherent property of separating the product CO_2 from flue gases. Instead of air, it uses an oxygen carrier, usually in the form of a metal oxide, to provide oxygen for combustion. All techniques so far proposed for chemical looping with solid fuels involve initially the gasification of the solid fuel in order for the gaseous products to react with the oxygen carrier. Here, the rates of gasification of coal were compared when gasification was undertaken in a fluidised bed of either (i) an active Fe-based oxygen carrier used for chemical looping or (ii) inert sand. This enabled an examination of the ability of chemical looping materials to enhance the rate of gasification of solid fuels. Batch gasification and chemical-looping combustion experiments with a German lignite and its char are reported, using an electrically-heated fluidised bed reactor at temperatures from 1073 to 1223 K. The fluidising gas was CO_2 in nitrogen. The kinetics of the gasification were found to be significantly faster in the presence of the oxygen carrier, especially at temperatures above 1123 K. A numerical model was developed to account for external and internal mass transfer and for the effect of the looping agent. The model also included the effects of the evolution of the pore structure at different conversions. The presence of Fe_2O_3 led to an increase in the rate of gasification because of the rapid oxidation of CO by the oxygen carrier to CO_2. This resulted in the removal of CO and maintained a higher mole fraction of CO_2 in the mixture of gas around the particle of char, i.e. within the mass transfer boundary layer surrounding the particle. This effect was most prominent at about 20% conversion when (i) the surface area for reaction was at its maximum and (ii) because of the accompanying increase in porosity and pore size, intraparticle resistance to gas mass transfer within the particle of char had fallen, compared with that in the initial particle. Excellent agreement was observed between the rates predicted by the numerical model and those observed experimentally.

1. Introduction

Hard coal and lignite are used to generate about 40.6% of the world's electricity, with natural gas providing 22.2%, oil 4.6%, nuclear 12.9%, hydro 16.0% and renewables 3.7% [1]. The demand for coal is expected to more than double by 2030 and it has been estimated [2] that about 4500 GW of new power plant (half in developing countries) will be required in this period. The implementation of modern, highly-efficient and clean technologies for the utilisation of coal is key to the development of economies if the effects of burning coal on society and environment are to be minimised. The principal means of controlling emissions of CO_2 from the use of coal will be to capture it from flue gases and sequester it in suitable geological structures. Such disposal is only feasible if the CO_2 is almost pure, largely free of nitrogen and other

* Corresponding author. Tel.: +44 1223 762962.
E-mail address: mas225@cam.ac.uk (M.A. Saucedo).

0016-2361/$ - see front matter © 2013 Elsevier Ltd. All rights reserved.
http://dx.doi.org/10.1016/j.fuel.2013.07.045

Nomenclature

A_A	coefficient in pressure gradient equation at arbitrary Knudsen number, Pa s m mol$^{-1.5}$
A_C	coefficient in pressure gradient equation in the continuum regime, Kn → 0, Pa s m mol$^{-1.5}$
A_K	coefficient in pressure gradient equation in the Knudsen regime, Kn → ∞, Pa s m mol$^{-1.5}$
A_{2ck_1}	pre-exponential factor for the rate constant $2ck_1$, mol s^{-1} g^{-1} bar^{-1}
A_{2ck_1}	pre-exponential factor for the rate constant $2ck_2$, mol s^{-1} g^{-1}
A_{k_{-1}/k_1}	pre-exponential factor for the rate constant k_{-1}/k_1, –
c	concentration of active sites per unit mass of carbon, g^{-1}
C_T	total concentration in the fluidized bed, mol m^{-3}
$D_{A,ab}$	diffusivity at arbitrary Knudsen number, involving species a and b, m^2 s^{-1}
$D_{B,ab}$	molecular diffusivity, involving species a in b, m^2 s^{-1}
$D_{K,a}$	Knudsen diffusivity of species a, m^2 s^{-1}
$D^{eff}_{B,ab}$	effective diffusivity in a fluidised bed, m^2 s^{-1}
$d_{b,m}$	mean diameter of a bubble, m
d_p	diameter of a particle, m
E_j	activation energy for the rate constant j, kJ mol^{-1}
$f(X)$	relative change in the surface area available for reaction over conversion, –
g	gravitational acceleration, m s^{-2}
ΔH	enthalpy of reaction, kJ mol^{-1}
H	expanded height of the fluidised bed, m
H_{mf}	height of the fluidised bed at minimum fluidisation, m
J_a	total flux of species a, mol m^{-2} s^{-1}
k_l	rate constant for the reaction of CO with iron oxide (Fe_2O_3), s^{-1}
k_1, k_{-1}	rate constants of gasification per active site, mol s^{-1} - bar^{-1}
k_2	rate constant of gasification per active site, mol s^{-1}
K_p	equilibrium constant for the overall gasification reaction C + CO_2 = 2CO, –
m_{batch}	mass of a batch of char, g
M_a	molecular mass of species a, kg
p_i	partial pressure of gaseous species i, bar
$p_{i,s}$	partial pressure of gaseous species i at the surface of the particle, bar
P	total pressure, bar
P_s	total pressure at the surface of the particle, bar
R_p	initial radius of a char particle, m
R	universal gas constant, kJ mol^{-1} K^{-1}
R_{pore}	radius of the pore, nm
R'_C	rate of conversion of carbon, mol s^{-1}
$R'_{Fe_2O_3}$	rate of reduction of the carrier with CO, bar s^{-1}
R'_g	rate of gasification of char per unit mass of sample, mol s^{-1} g^{-1}
$R'_{g,0}$	intrinsic rate of gasification of char at zero conversion, mol s^{-1} g^{-1}
Re_p	Reynolds number in the particulate phase, –
S_0	initial internal surface area of the particle per unit volume, m^2 m^{-3}
Sh	Sherwood number, –
t	time, s
T	temperature, K
U	superficial fluidising velocity, m s^{-1}
U_B	rise velocity of a bubble, m s^{-1}
U_{mf}	minimum superficial fluidising velocity, m s^{-1}
X	conversion of carbon, –
X_f	cross-flow factor, –
y_i	mole fraction of species i, –
$y_{i,bulk}$	mole fraction of species i in the fluidising gas (or bulk phase), –
$y_{i,s}$	mole fraction of species i at the surface of the particle, –

Greek letters

δ	thickness of the mass transfer boundary layer, m
ε_o	initial porosity of the char, –
ε_b	void fraction owing to bubbles in the fluidised bed, –
ε_{ext}	porosity of the region around the particle of pellet, –
ε_{mf}	void fraction in a bed at minimum fluidisation, –
η_{in}	effectiveness factor of the extent of mass transfer limitations within the particle, –
μ_a	dynamic viscosity of species a, Pa s
μ_{mix}	effective viscosity of the mixture of the gas, Pa s
ν	kinematic viscosity, m^2 s^{-1}
ρ_e	density of a particle of char before reaction, g m^{-3}
σ_r	dimensionless radius, defined as r/R_p, –
τ^2_{ext}	tortuosity factor of the region around the particle of pellet, –
τ^2_{in}	tortuosity factor of the particle, –
υ_a	stoichiometric coefficient of species a
φ_c	mass fraction of carbon in the char, –

Subscripts

a = 1	CO
a = 2	CO_2
a = 3	N_2

Abbreviations

CLC	chemical-looping combustion
BET	Brunauer–Emmett–Teller
MeO	metal oxide

gases [3]. Chemical looping combustion (CLC) of coal can produce relatively pure CO_2 without costly separation processes.

CLC for gaseous fuels involves two interconnected fluidised beds; the fuel, C_nH_{2m}, enters the *fuel reactor*, where it reacts with an oxygen carrier, typically a metal oxide (MeO): $(2n + m)MeO + C_nH_{2m} \rightarrow (2n + m)Me + mH_2O + nCO_2$ (*a*), producing largely CO_2 and steam, yielding almost pure CO_2 when the steam is condensed. The reduced metal oxide, Me, is transferred to the *oxidation reactor*, where it is oxidised: $Me + 1/2O_2 \rightarrow MeO$ (*b*). The oxidised MeO is recycled to the first reactor to begin a new cycle of reduction and oxidation. Full conversion from MeO to Me and *vice versa* is not necessarily obtained in a real system, neither is it essential [3,4]. The exit gas from the oxidation reactor is N_2 containing unused O_2. Taking reactions (*a*) and (*b*) together, the fuel has been combusted but the CO_2 has been kept separate from the N_2 in the air. Depending on the metal oxide, the enthalpy change associated with (*a*) is often, but not always small: reaction (*b*) is always exothermic. When the two reactors are fluidised beds, and where reaction (*a*) is endothermic, the interchange of the solid oxygen carrier between the beds can be used to provide heat to the fuel reactor. The heated, depleted air leaves the oxidation reactor at high temperature (*ca.* 1273 K) and can be used to raise steam,

Table 1
Thermodynamic information for selected reactions [33].

Reaction	ΔH^0_{1173K}/kJ mol^{-1}	ΔG^0_{1173K}/kJ mol^{-1}	
$3Fe_2O_{3(s)} + CO_{(g)} \rightarrow 2Fe_3O_{4(s)} + CO_{2(g)}$	−38.6	−108.2	(2)
$0.947Fe_3O_{4(s)} + 0.788CO_{(g)} \rightarrow 3Fe_{0.947}O_{(s)} + 0.788CO_{2(g)}$	+16.7	−5.5	(3)

or, when the operation is pressurised, to drive a gas turbine topping cycle [5]. This technique for the combustion of gaseous fuels, particularly natural gas, has been an active research area for the last two decades, with work on oxygen carriers [5–9], reactor design [3,4,10,11] and thermodynamic efficiency [12–16]. There have been significant advances towards industrial demonstration with gaseous fuels [10,17].

In contrast to gaseous fuels, the use of CLC with solid fuels is complicated because the particles of fuel and oxygen-carrier cannot be easily separated [5,18–35]. Without separation, solid fuel would enter the oxidation reactor with the recycled oxygen carrier, its combustion causing CO_2 to contaminate the depleted air stream, and decreasing capture efficiency. To circumvent this, three broad approaches have evolved [5]. The first would be to gasify the solid fuel and burn the resulting synthesis gas in a separate reactor using conventional chemical looping. The second would be to gasify the solid fuel in pure CO_2 or steam, or mixtures thereof, *in situ* in the presence of the metal oxide so that the resulting synthesis gases, and any volatile matter, react with the adjacent carrier particles. Additionally, the unburnt char would be separated from the spent oxide before the carrier solids are recycled to the oxidation reactor. The third approach would involve gasification *in situ* in a cyclic batch operation. For the first approach, in order to obtain undiluted syngas, the gasification would have to be performed with O_2, thus requiring an air separation unit (ASU). In contrast, no additional ASU is needed with the other techniques. However, the solid–solid reaction between char and a metal oxide does not occur at an appreciable rate [24,28]. Instead, the solid fuel needs to be gasified *in situ* to form synthesis gas, which is subsequently oxidised by the oxygen-carrying particles: generally, the gasification is rate-limiting [22–24,28].

To illustrate the use of iron oxide as an oxygen carrier, consider gasifying carbon char by CO_2, thus:

$$C_{(s)} + CO_{2(g)} \rightarrow 2CO_{(g)} \quad \Delta H^0_{1173\ K} = +173\ \text{kJ mol}^{-1}. \tag{1}$$

This reaction is followed by Reaction (2) in Table 1, giving a net enthalpy of +95.8 kJ mol^{-1} for complete conversion of the char. Reaction (2) will occur at 1173 K provided $p_{CO}/p_{CO_2} > 1.5 \times 10^{-5}$ [33]; however, for the subsequent reduction of Fe_3O_4 to $F_{0.947}O$ in Reaction (3) at the same temperature, $p_{CO}/p_{CO_2} > 0.6$, giving incomplete combustion. Accordingly, only the reduction to Fe_3O_4 (magnetite) is likely to be possible in combusting systems.

An important advantage in a chemical-looping reactor is that gasification will take place in an atmosphere with a high concentration of CO_2 and, or, H_2O, whilst CO and H_2, which inhibit gasification, are consumed by reaction with the oxygen carrier [34–37]. Thus, the rate of gasification should be faster in a chemical-looping system than in a normal gasifier. The aim of this study was to investigate experimentally the effect on the rate of gasification of the chemical looping agent (in this case iron oxide). A numerical model was developed, which included the intrinsic kinetics and mass transfer limitations within and surrounding the particle of gasifying char, to explain the observed enhancement in gasification rates in the chemical looping system.

2. Theory

2.1. Kinetics of gasification with CO_2

The most widely-accepted mechanism for gasification in Reaction (1) is the oxygen-exchange scheme [38] involving the adsorption of CO_2 on an active site on the char, C^*

$$C^* + CO_{2(g)} \underset{k_{-1}}{\overset{k_1}{\leftrightarrow}} C(O) + CO_{(g)} \tag{4}$$

followed by the desorption of the product CO

$$C(O) \xrightarrow{k_2} C^* + CO_{(g)}. \tag{5}$$

Hence, $R'_{g,0}$, the initial rate of formation of CO per unit mass of carbon, in the absence of external mass transfer, can be related to the partial pressures of CO and CO_2:

$$R'_{g,0} = \frac{2ck_2\left(p_{CO_2,s} - \frac{p^2_{CO,s}}{K_p}\right)}{p_{CO_2,s} + (k_2/k_1) + (k_{-1}/k_1)p_{CO,s}}, \tag{6}$$

an equation originally proposed by Ergun [38], modified here with an extra term $\frac{p^2_{CO,s}}{K_p}$ to give the correct behaviour close to equilibrium, i.e. allowing Reaction (5) to be reversible [34,5]. Here, k_1, k_{-1} and k_2 are the rate constants per active site, c is the concentration of active sites per unit mass of sample, K_p is the equilibrium constant for Reaction (1) and $p_{i,s}$ is the partial pressure of species i at the surface of the particle. The equilibrium constant k_{-1}/k_1 for three types of carbon is best given by [38]:

$$k_{-1}/k_1 = 2.4 \times 10^{-4} \exp[-E_{k_{-1}/k_1}/RT] \tag{7}$$

with the activation energy $E_{k_{-1}/k_1} = -95$ kJ/mol, although it varies somewhat with the type of carbon [34]. The activation energy of $2ck_2$ was found to be independent of the type of carbon [38], with the primary difference in reactivity among carbons arising from the number of available active sites, c, rather than from differences in the intrinsic kinetic constants. Since there is no evidence of direct chemisorption of CO, it is probable that inhibition occurs by the reverse of Reaction (4) [35]. The value of k_2 has been measured in transient experiments [39,40] and found to be independent of p_{CO_2}, thereby providing evidence for the Langmuir–Hinshelwood mechanism leading to Eq. (6). It should be noted that it is impossible to measure an intrinsic rate constant, i.e. the rate per active site on the carbon's surface, without an independent measurement of the concentration, c, of active sites [38,39].

As a particle of char undergoes gasification, a growth in the rate of reaction is normally observed during the initial phase of the reaction. This is largely attributed to the increase in the surface area available for reaction as the pores increase in size [41]. In order to account for this effect, the rate of reaction at an average conversion, $R'_g(X)$, can be expressed as

$$R'_g(X) = R'_{g,0} \times f(X) \tag{8}$$

where $f(X)$ is a function representing the relative change in the surface area available for reaction as a function of the average conversion of the particle of char.

Of course, the observed kinetics will reflect the intrinsic kinetics only in the absence of any mass transfer limitations, arising either within the pores of a gasifying fuel particle or by transfer between the bulk gas surrounding a particle and its external surface. This is illustrated in Fig. 1, where intraparticle diffusion occurs in region R-I and external mass transfer occurs in R-II.

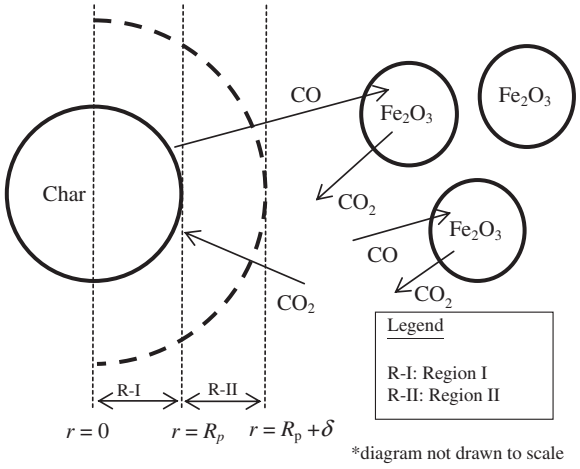

Fig. 1. Schematic diagram of the gasification of char in CO_2 to produce CO. CO is then consumed by Fe_2O_3, the chemical looping agent, to produce CO_2.

2.2. Intraparticle mass transfer

Here, a porous particle of char (reacting with intrinsic chemical kinetics described by Reaction (1)) is assumed to be homogeneous so that c in Eq. (6) is uniform throughout. Such an assumption is reasonable if steep concentration gradients within the particle are absent. Since the stoichiometry of the reaction is non-equimolar, and three species are involved (including N_2 as the inert), simple binary diffusion cannot be assumed. It was found that when a simple binary diffusion model was applied, an error of approximately 10% was incurred for the concentrations at the centre of the particle. It is also noted that the use of a binary diffusion model for a non-equimolar counter diffusion problem leads to an inconsistency where the total mole fraction does not sum to unity at any normalised radius less than unity. Here diffusion and advective transport within the particle is described using the Cylindrical Pore Interpolation Method (CPIM), a multicomponent flux model based on the Stefan–Maxwell equations, modified by a momentum balance [42]. A discussion on the application of the CPIM for a spherical, porous catalyst can be found elsewhere [43]. Within the spherical particle of char, the material balance equations are

$$\frac{1}{r^2}\frac{d}{dr}(r^2 J_a) = \frac{v_a}{2} R'_g(X)\rho_e \tag{9}$$

where r is the radius within the particle, $R'_g(X)$ is the rate of gasification at the local gas concentration but average conversion X, in mol s^{-1} g^{-1} and given by Eq. (8), J_a is the total flux of species a, v_a is the stoichiometric coefficient of species a and ρ_e is the initial density of the particle of char before it has reacted. It should be noted that the total flux, J_a, will be used consistently in this study and represents the sum of the diffusive and advective fluxes. The factor of 1/2 was included because the rate in Eq. (6) is expressed as the production of CO. Here, $a = 1$ is taken to refer to CO, 2 to CO_2 and 3 to N_2. It should be noted that a simplifying assumption has been made to make $R'_g(X)$ dependent on the average conversion of the whole particle, whereas, more rigorously, it should be a function of the local conversion, which will vary across the radius of the particle because there is a radial gradient in gas concentrations owing to the resistance to intraparticle mass transfer. The validity of this assumption is discussed later in Section 5.3. Finally, it is assumed that there is only one chemical reaction, i.e. Eq. (6), and N_2 is inert, therefore

$$J_1 = -2J_2 \text{ and } J_3 = 0. \tag{10}$$

Using the CPIM [42] and Eq. (10), the following equations were used to describe gaseous transport within the porous structure of the particle of char.

$$\frac{dy_1}{dr} = \frac{\tau_{in}^2 RT}{\varepsilon P}\left[\frac{y_1 J_2}{D_{A,21}} - \frac{y_2 J_1}{D_{A,12}} - \frac{y_3 J_1}{D_{A,13}}\right] \tag{11}$$

$$\frac{dy_2}{dr} = \frac{\tau_{in}^2 RT}{\varepsilon P}\left[\frac{y_2 J_1}{D_{A,12}} - \frac{y_1 J_2}{D_{A,21}} - \frac{y_3 J_2}{D_{A,23}}\right] \tag{12}$$

$$\frac{dy_3}{dr} = \frac{\tau_{in}^2 RT}{\varepsilon P}\left[\frac{y_3 J_1}{D_{A,13}} + \frac{y_3 J_2}{D_{A,23}}\right] \tag{13}$$

$$\frac{dP}{dr} = -\frac{\tau_{in}^2 A_A}{\varepsilon}\left(J_1\sqrt{M_1} + J_2\sqrt{M_2}\right) \tag{14}$$

where y_a and M_a are the mole fraction and molecular mass of species a, ε is the porosity of the particle, τ_{in}^2 is the tortuosity factor of the particle and P is the total pressure. Eq. (14) indicates that there will be a variation of total pressure within a reacting particle, a factor which has often been neglected. It is noted that the omission of Eq. (14) would not alter the conclusion of this study. However, pressure variations would be more significant if the char were to have a higher reactivity and smaller pore sizes were involved. The parameters $D_{A,ab}$ and A_A were found by interpolating between the extremes of continuum and Knudsen flow using [42]:

$$\frac{1}{D_{A,ab}} = \frac{1}{D_{K,a}} + \frac{1}{D_{B,ab}} \tag{15}$$

$$\frac{1}{A_A} = \frac{1}{A_K} + \frac{1}{A_C} \tag{16}$$

where $D_{K,a}$ and $D_{B,ab}$ are the Knudsen diffusivity and the molecular diffusivity, respectively. In the present work, the molecular diffusivities were calculated using the equation of Fuller et al. [44] and Knudsen diffusivities using kinetic theory [45]. The parameters A_K and A_C are the coefficients in the pressure gradient equation in the continuum and Knudsen regime, respectively, given by

$$A_K = \frac{3}{4R_{pore}}\left(\frac{\pi RT}{2}\right)^{1/2} \tag{17}$$

$$A_C = \frac{8\mu_{mix}RT}{PR_{pore}^2\sum_{b=1}^{3} y_b M_b^{1/2}} \tag{18}$$

where R_{pore} is the radius of the pore and μ is the effective viscosity of the mixture of gases. The dynamic viscosities of CO_2 and N_2, the two main species present in the system, are 4.41×10^{-5} and 4.61×10^{-5} Pa s. Since these values are very similar, the viscosity of the mixture was taken to be a constant in the solution of the model and was approximated to be 4.58×10^{-5} Pa s by the following relationship:

$$\frac{1}{\mu_{mix}} = \frac{y_2}{\mu_2} + \frac{y_3}{\mu_3}. \tag{19}$$

The analysis was found to be insensitive to the value of viscosity.

By setting $a = 1$ in Eq. (9) the profiles of composition and total pressure within the particle of char can be obtained by solving Eq. (9) with Eqs. (11)-(14). The boundary conditions are

$$r = 0 \quad J_1 = 0 \tag{20}$$

$$r = R_p \quad J_a = J_{a,s}, \quad P = P_s \text{ where a} = 1, 2, 3 \tag{21}$$

where $y_{a,s}$ and P_s are, respectively, the mole fraction of species a and the total pressure at the surface of particle.

2.3. External mass transfer model

It is also important to consider the effect of external mass transfer around the reacting particle of char, *viz.* Region II in Fig. 1, in order to understand the effect of the looping agent on the gasification of char. The approach will be based on the Stefan–Maxwell equations, involving the non-equimolar counter diffusion of CO_2 and CO in N_2, as presented by [5]. The net average mass flux of material leaving the particle of char was found experimentally to be small

and the permeability of the particulate phase is large enough to allow pressure variations resulting from this flux to be neglected: this is discussed further in Section 5.2.

The material balance for the boundary layer around the particle of char, i.e. from $r = R_p$ to $r = R_p + \delta$, can be described by

$$\frac{dJ_1}{dr} = -\frac{2}{r}J_1 - \frac{R'_{Fe_2O_3}}{RT} \tag{22}$$

where $R'_{Fe_2O_3}$ is the rate of reaction of CO with Fe_2O_3, described by Reaction (2) and R_p is the radius of the reacting particle of char. This neglects the transient terms in the balance since the time constant for the steady state profile to become established is fast compared with the time scale for particle conversion, permitting a pseudo-steady analysis. The rate of reduction of the carrier was taken to be first order in gaseous reductant, such that

$$R'_{Fe_2O_3} = k_l p_1 \tag{23}$$

based on unit volume of particulate phase. The values of the first-order rate constant k_l for the carrier used in this work at the different temperatures have been determined experimentally [46] for the reduction of Fe_2O_3 to Fe_3O_4 by CO. It should be noted that Eq. (22) can be used to describe the material balance when the particles of char were gasified either with sand or with looping agent except that in the former $R'_{Fe_2O_3} = 0$. The Stefan–Maxwell equations for the fluxes of CO and CO_2 in the boundary layer are

$$\frac{dy_1}{dr} = \frac{RT}{P}\left[\frac{y_1J_2 - y_2J_1}{D^{eff}_{B,12}} - \frac{y_3J_1}{D^{eff}_{B,13}}\right] \tag{24}$$

$$\frac{dy_2}{dr} = \frac{RT}{P}\left[\frac{y_2J_1 - y_1J_2}{D^{eff}_{B,12}} - \frac{y_3J_2}{D^{eff}_{B,23}}\right] \tag{25}$$

$$\frac{dy_3}{dr} = \frac{RT}{P}\left[\frac{y_3J_1}{D^{eff}_{B,13}} + \frac{y_3J_2}{D^{eff}_{B,23}}\right] \tag{26}$$

with $J_3 = 0$ and $J_2 = -0.5\,J_1$. Here, the effective diffusivity, $D^{eff}_{B,ab}$, is given by

$$D^{eff}_{B,ab} = \frac{\varepsilon_{ext} D_{B,ab}}{\tau^2_{ext}} \tag{27}$$

where ε_{ext} and τ^2_{ext} is the porosity and tortuosity factor of the region around the particle of fuel immersed in the particulate phase of the fluidised bed. The boundary conditions for the solution of Eqs. (22) and (24)–(26) are

$$r = R_p \quad J_1 = J_{1,s} \tag{28}$$

$$r = R_p + \delta \quad y_a = y_{a,bulk} \text{ where } a = 1, 2, 3. \tag{29}$$

where $y_{a,bulk}$ is the mole fraction of species a in the fluidising gas and δ is the thickness of the mass transfer boundary layer.

3. Experimental

3.1. Materials

3.1.1. Fuel and preparation of the char

A low-rank Hambach lignite coal, supplied by RWE Power AG, Germany, and its char were investigated in this work. The ultimate and proximate analyses are shown in Table 2. On an 'as received' basis (ar), the Hambach lignite coal had a high content of moisture. Therefore, prior to its use, the lignite was dried in an oven for 24 h at 353 K. Based on the mass of coal before, and after, drying, the lignite showed a decrease of mass of 53 wt.%; this is consistent with the total content of moisture measured in the proximate analysis of 54.1 wt.%. Lignite char was prepared from its parent lignite by pyrolysis in nitrogen in a fluidised bed of sand at 1073 K. The reactor had an inside diameter of 78 mm and was made from 316 stainless steel. A detailed description of the apparatus and the experimental method have been given elsewhere [5,28]. The lignite coal and its char were sieved to the desired size fraction, usually +710, −1000 or +600, −1000 μm, respectively, unless otherwise stated.

3.1.2. Preparation of oxygen carrier

Iron oxide particles were prepared by the method of mechanical mixing described elsewhere [47]. Briefly, this entails spraying Fe_2O_3 powder (Sigma–Aldrich, < 5 μm and >99 wt.% purity) with reverse osmosis water and mixing manually to form small agglomerates. These were gently sieved to +300, −425 μm and then placed in crucibles and calcined in a muffle oven at 1223 K for 3 h. Once cooled, the particles were further sieved to the desired size fraction of +300, −425 μm; about 35% of the calcined particles had a size fraction below 300 μm. The particle density, as measured by helium pycnometry, was ~5380 kg m^{-3}. The fresh particles of iron oxide had a BET area of ~1 m^2 g^{-1}. It has been shown in [48] that carriers do not need a high surface area to be active, provided there is sufficient macroporosity.

Experiments were also undertaken in the absence of an oxygen carrier by replacing it with inert, uncrushed silica sand (fraction C, David Ball Group plc, moisture content <0.1% by dry mass, BS 1881-131:1998), sieved to a size fraction of +300, −425 μm. The density of the sand was ~2690 kg m^{-3}.

3.2. Apparatus and method

Batch experiments were performed in a fluidised bed contained in a quartz reactor, of internal diameter 30 mm and length 460 mm, provided with a porous frit (4 mm thick, pore size +100, −160 μm) as the distributor (with pressure drop sufficient to ensure uniform fluidisation), situated 110 mm from the base of the reactor. A schematic diagram of the general arrangement of this apparatus is shown in Fig. 2. The reactor was externally heated by an electric furnace (LTF 12/38/250, Lenton Thermal Designs Ltd.) with a maximum temperature of 1273 K. The temperature of the bed was measured by a K-type thermocouple (1.5 mm dia.) inserted into the top of the bed. Gas was supplied through a connection at the base of the reactor. The flow rates of air, nitrogen, carbon dioxide and carbon monoxide (from gas cylinders supplied by BOC plc or Air Liquide) were controlled with rotameters calibrated at 293 K and 1 bar. Solenoid valves enabled mixtures of the gases to be made and allowed for easy switching between gas streams. A fraction of the off-gases leaving the reactor was sampled through a right-angled quartz probe, inserted into the top of the reactor. The gas sample was pumped at a rate of 16.7 mL s^{-1} as measured at ambient temperature and pressure. In order to prevent any elutriated particles, tars and water vapour in the sample gas entering the infrared analysers the sample gas was passed through (i) a glass wool filter; (ii) an impinger tube submerged in ice bath and (iii) a drying tube filled with $CaCl_2$ pellets. The gas concentrations were measured with a non-dispersive, infra-red gas analyser (ABB EL3020) used for measuring CO_2, CO and SO_2 coupled with a paramagnetic analyser (Magnos206) to measure O_2. Hydrogen was measured using a thermal conductivity analyser (ABB EL3020-Caldos 27). The sampling system, including the gas analysers, was corrected for mixing effects by measuring the response time of the analysers to a step change in the concentration. This procedure has been described elsewhere [28]. Briefly, the sampling system was modelled as a plug flow reactor in series with a continuous stirred tank. The sampling system followed a first-order response, giving a time constant of ~4.6 s. It will be seen later that the time constant for gasification of lignite char was substantially longer than this value.

Table 2
Proximate and ultimate analyses of fuel investigated (ar = as received, wd = mass dry).

	Hambach lignite coal		Hambach lignite char
	ar	wd	
Proximate analysis			
Total moisture (wt.%)	54.1	–	ND
Ash content (wt.%)	2.12	5.52	8.76
Volatile matter (wt.%)	22.2	50.7	ND
Sulphur (wt.%)	0.14	0.31	0.6
Fixed carbon (wt.%)	19.9	45.6	ND
Lower heating value (kJ kg^{-1})	10,065	26,003	ND
Ultimate analysis			
Carbon (wt.%)	30.6	54.91	85.69
Hydrogen (wt.%)	2.4	5.47	0.82
Nitrogen (wt.%)	0.41	0.93	0.84
Oxygen (balance) (wt.%)	58.4	32.86	3.3

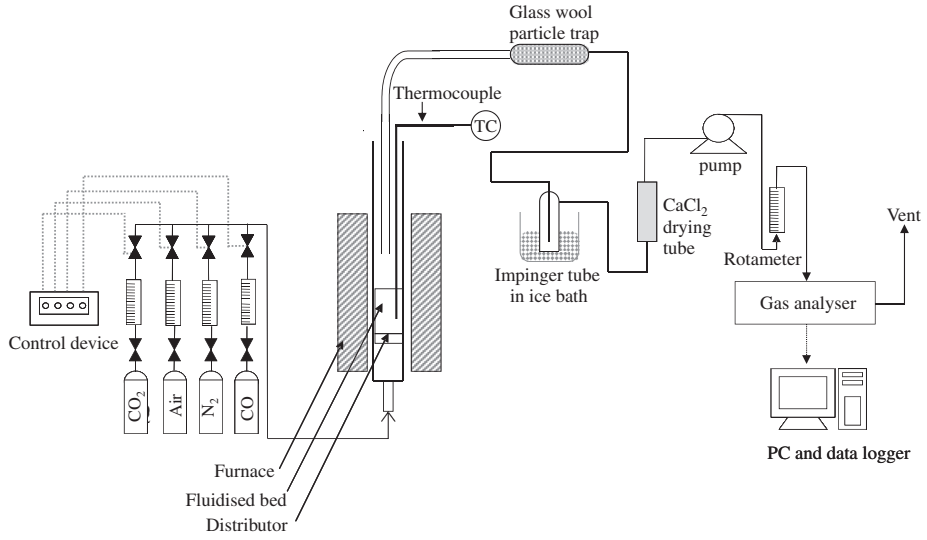

Fig. 2. Schematic experimental setup for batch experiments in a quartz reactor.

In a typical experiment, the reactor was filled with 33 g of either silica sand or iron oxide particles and then heated to the desired temperature, *viz.* 1048 - 1248 K. For the gasification stage (and further reduction of the iron oxide, when present), the mole fraction of CO_2 in the fluidising gas was typically 12.5 mol.% with the balance nitrogen. The total volumetric flow rate was 50 mL s^{-1} (at 293 K, 1 bar), giving $U/U_{mf} \sim$ 5.2–6.0 for the sand, and ~2.6–3.0 for the experiments with the looping agent, with U being the superficial velocity at the temperature of the bed and U_{mf} the superficial velocity at incipient fluidisation, calculated from the correlation of Wen and Yu [49]. Then, a known mass of fuel, usually 0.15 g, was added to the reactor and allowed to gasify completely. Every experiment was repeated at least 3 times. The amount of fuel added to the bed was adjusted to ensure that the maximum conversion of CO_2 to CO after the batch had been added was below 5%, so as to avoid complications arising from mass transfer between the bubble and the particulate phases. For experiments with iron oxide particles present, complete conversion of 0.15 g of fuel to CO_2 is equivalent to an approximate conversion of 31% of the iron oxide particles from Fe_2O_3 to Fe_3O_4, i.e. reduction to FeO, or Fe, was not possible owing to an excess of haematite. The time for the batch burn-out of fuel was typically between 600 and 3600 s. After the gasification period was complete, nitrogen was introduced for 180 s followed by the oxidation period in which the reduced iron oxide and any remaining unburnt char were oxidized in 3.67 mol.% O_2, balance N_2. Here, air diluted with nitrogen was used instead of air in order to limit the temperature increase arising from the exothermic oxidation of Fe_3O_4. The total volumetric flow rate during the oxidation step was 46.7 mL s^{-1} (at 293 K and 1 bar), giving $U/U_{mf} \sim$ 4.2–4.8 for the sand, and ~2.1–2.4 for the experiments with the looping agent.

Irrespective of the bed material used, a carbon balance gives

$$R'_C = \dot{n}_{out}(y_{CO,out} + y_{CO_2,out}) - \dot{n}_{in}(y_{CO,in} + y_{CO_2,in}) \quad (30)$$

where R'_C is the rate of carbon conversion in mol s^{-1}: $\dot{n}_{out}$ and $\dot{n}_{in}$ are the total molar flows leaving and entering the reactor, respectively, with $\dot{n}_{out} = \dot{n}_{in}(1 - y_{CO,in} - y_{CO_2,in}) + \dot{n}_{out}(y_{CO,out} + y_{CO_2,out})$. In all experiments, the normalised rate of production of carbon monoxide (or equivalently, for the experiments in Fe_2O_3, the rate of generation of CO by the gasification reaction, assuming carbon only enters the gas phase *via* Reaction (1)), R'_g (mol s^{-1} g^{-1}), was given by

$$R'_g = \frac{2 \times R'_C}{m_{batch}} = 2 \times \left[\frac{\dot{n}_{out}(y_{CO,out} + y_{CO_2,out}) - \dot{n}_{in}(y_{CO,in} + y_{CO_2,in})}{m_{batch}}\right] \quad (31)$$

where m_{batch} is the initial mass of char added. The mole fraction of CO in the gas entering the reactor, $y_{CO,in}$, was typically zero. However, in some experiments, a small fraction of CO was added to

the inlet gas to quantify the inhibitory effect of CO on the intrinsic kinetics of gasification of lignite char. Finally, the rate of carbon conversion for a char with mass fraction of carbon φ_C, was defined as

$$\frac{dX}{dt} = \frac{6R'_g}{\phi_C}. \quad (32)$$

4. Results

4.1. Cross-flow from the bubble to the particulate phase

The mass of a batch of char, m_{batch}, used in an experiment had to be chosen to be small enough to ensure that the transfer of gas from the bubble phase of the bed to the particulate phase did not influence the rate of gasification and not so small as to render deviations in the concentrations in the off-gas indistinguishable from the background. This was verified by performing experiments in which progressively larger batches of Hambach lignite char with masses between 0.02 and 0.15 g, were added to a bed of sand at 1073 K at a fixed concentration of 86 mol.% CO_2 in N_2. Fig. 3 shows that, over this range, the rate of production of CO was proportional to the mass of char indicating that, for batches in this range of mass, cross-flow between the bubble and the particulate phases did not limit the reaction.

For experiments with beds of Fe_2O_3 (Sections 4.1–4.5), all of the CO produced by gasification was oxidised to CO_2 by the time it left in the off-gases; using a relatively large batch of $m_{batch} \sim 0.15$ g maximised the deviation between the inlet and outlet concentrations of CO_2, thereby reducing the error associated with calculating rates of reaction. However, for the experiments with beds of sand used to determine the intrinsic kinetics of the gasification of lignite char, it was found that a smaller batch of ~0.05 g sufficed.

To support the conclusions from Fig. 3, the bubble to particulate phase resistance of the fluidised bed was estimated [50] by calculating the bed cross-flow factor, X_f, defined as the number of times the bubble gas is replaced on passage of bubble through the bed. As X_f becomes large (>3, say), the difference in concentration between gas in the particulates phase and that in the bubble phase becomes negligible. For Group B particles, X_f is given by [50]

$$X_f = \frac{6.34 H_{mf} U_{mf}}{d_{b,m}(g d_{b,m})^{1/2}} \quad (33)$$

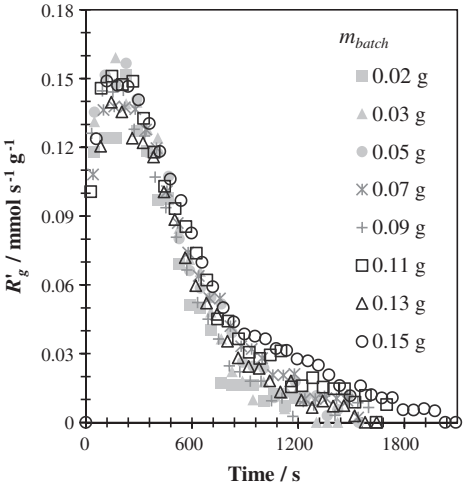

Fig. 3. Gasification of different batches of Hambach lignite char, d_p = 600–1000 μm, at 1073 K in 86 mol.% CO_2 in N_2 showing the rate of production of CO per unit mass of batch. Total volumetric flow rate was 50 $cm^3\ s^{-1}$ (293 K, 1 bar). Batch masses between 0.02 and 0.15 g.

where H_{mf} is the height of the bed at minimum fluidisation, g is the gravitational acceleration, and $d_{b,m}$ is the mean diameter of a bubble, determined from the correlation of [51]

$$d_{b,m} = \frac{0.54(U - U_{mf})^{0.4}(h + 4\sqrt{A_0})^{0.8}}{g^{0.2}} \quad (34)$$

with h = height of the bed above the distributor and A_0 = (area of distributor plate)/(no. of orifices). $A_0 \sim 0$ for a bed with a porous plate distributor and the mean size diameter of a bubble was assumed to be about 50% the size at height H. For the experiments in a bed of sand, X_f was 3.1, 2.9 and 2.6 at 1073, 1123 and 1173 K, respectively. For the bed of Fe_2O_3, X_f was, respectively, 8.3, 7.4 and 6.7, owing to the higher U_{mf} for particles of Fe_2O_3 than sand, i.e. $U_{mf,Fe2O3} \approx 2 \times U_{mf,sand}$. The high cross-flow factor in all experiments suggests complete mixing within the whole bed.

4.2. Kinetics of gasification: reproducibility with cycling

Fig. 4(a) shows the typical measured mole fractions of CO_2 and CO in the exit gas during the gasification of a batch of lignite char at 1073 K in 12.5 mol.% CO_2, balance N_2, in both a bed of sand and a bed of iron oxide. In this case, all CO produced during the gasification of the char was oxidised by the MeO to CO_2. The char was allowed to gasify for 3600 s and was followed by purging the reactor in N_2 for 180 s and by the oxidation step. A typical profile of the measured mole fractions of CO_2 and O_2 in the exit gas during these last two steps is shown in Fig. 4(b). In this step (i) any remaining char inventory in the reactor was burnt and (ii) the Fe_3O_4 was re-oxidised fully back to Fe_2O_3. The temperature in the bed during the re-oxidation step rose, typically, between 4 and 12 K, depending on the amount of char present in the bed and the amount of magnetite to be oxidised, owing to both reactions being highly exothermic. The delay of the mole fraction of O_2 during the re-oxidation step when iron oxide is present corresponds to the very rapid oxidation of Fe_3O_4 with O_2 and with negligible escape of oxygen to the freeboard. Each of these three steps together in Fig. 4(a) and (b) represented one cycle.

The stability of the iron oxide particles used in this paper was tested over a period of 15 cycles of reduction and oxidation to determine whether or not the measured rates were affected by cycling the carrier particles. Ideally, a fresh bed of iron oxide would have been used before each gasification experiment, but, for simplicity, the particles were reused during a single day of operation. The net rate of production of CO_2 per unit mass of carbon, $(\dot{n}_{out} \cdot y_{CO_2,out} - \dot{n}_{in} \cdot y_{CO_2,in})/m_{batch}$, during the reduction step of six different batches of Hambach lignite coal in an initially fresh bed of Fe_2O_3 is shown in Fig. 5(a). The rate of reaction is very similar for all cycles showing a maximum rate at time ~9.5 ± 0.8 s from the start of reaction. After ~40 s, most gases from the devolatilisation step have been driven off, to be followed by the much slower reaction of the remaining char, with a duration of ~260 s. The concentration profiles in the purging and re-oxidation stages (not shown in this figure for simplicity) were very similar for all cycles. The iron oxide was found to have been partially reduced from haematite to magnetite by 22.5 ± 0.4 mol.%, as determined by the oxygen consumption during the oxidation step. No remaining char was observed in the bed during this step, indicating that the batches of coal reacted to completion during the reduction step. Fig. 5(b) shows the maximum rate observed for all 15 cycles during the devolatilisation stage and the rate of reaction at $t \sim 40$ s, corresponding to the "initial" rate of reaction of the char. The maximum net rate of production of CO_2 was ~0.70 mmol s^{-1} g^{-1} with a standard deviation of ±0.03 mmol s^{-1} g^{-1}, representing about 4.6% of the average value. The corresponding rate for char gasification was ~0.19 mmol s^{-1} g^{-1} with a standard deviation of

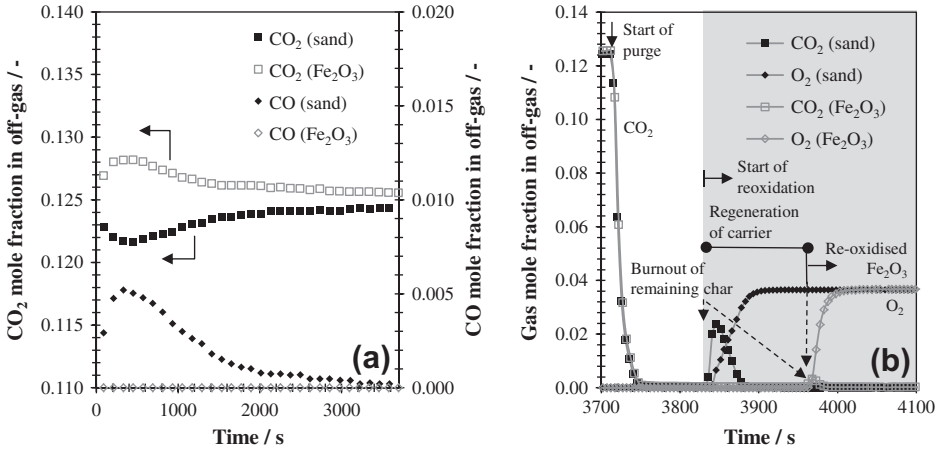

Fig. 4. Comparison of the typical molar concentration profile in the exit gas during one cycle of a batch experiment with lignite char, $m_{batch} \sim 0.15$ g, at 1073 K in a bed of sand or a bed of Fe_2O_3 as oxygen carrier. (a) *Reduction step*: gasification of the solid fuel in 12.5 mol.% CO_2, balance N_2. (b) *Purging and oxidation steps*: purge in N_2 for 180 s followed by re-oxidation of Fe_3O_4 and combustion of any remaining char in 3.67 mol.% O_2, balance N_2.

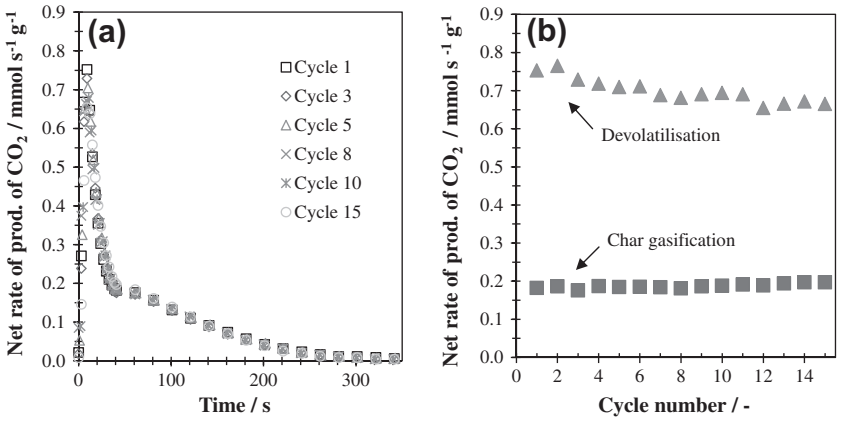

Fig. 5. Net rate of production of CO_2 of different cycles in a bed of Fe_2O_3 at 1123 K during the gasification of Hambach lignite coal, when fluidised with 12.5 mol.% CO_2, balance N_2. Total volumetric flow rate was 50 $cm^3\ s^{-1}$ (as measured at 293 K, 1 bar). (a) Rate over time showing the initial degassing stage (first ~40 s) and the burning of the remaining char ($40 < t < 320$ s). (b) Maximum rate observed during devolatilisation of the coal at $t \sim 9.5 \pm 0.8$ s (▲) and the rate observed just after devolatilisation at $t \sim 40$ s (■).

±0.006 mmol s^{-1} g^{-1}. These results indicate that the experiments were not affected by cycling of the iron oxide particles, at least during the first 15 cycles. Thus, all experimental results presented in this paper where iron oxide was involved were carried out with particles which had been cycled 15 times or fewer.

4.3. Reaction of Hambach lignite coal

Fig. 6 shows further details of the mole fractions of species in the off-gas during the gasification of Hambach lignite coal at 1073 K in a bed of (a) pure silica sand and (b) Fe_2O_3. For a bed of sand (Fig. 6(a)), during the initial period of devolatilisation, a large peak of CO was observed, together with some H_2. It is possible that hydrocarbons were also present in the off-gas, although the means to measure them in these experiments was not available. However, when the iron oxide was present, Fig. 6(b), all the CO produced during the gasification of the coal is immediately oxidised by the Fe_2O_3 to CO_2. Also, practically no H_2 was observed during the devolatilisation of the coal, indicating that the Fe_2O_3 was also oxidising the H_2 to H_2O. Neither CO_2 nor CO was observed during the oxidation step with either iron oxide or sand present, indicating that the gasification reaction was completed before ~1200 s.

4.4. Effect of temperature

Fig. 7 compares (a) the rates of production of CO, R'_g and (b) conversion of the fuel as functions of time during the gasification of Hambach lignite char at three different temperatures, i.e. 1073, 1123 and 1173 K, in a bed of sand and in a bed of Fe_2O_3. No CO was observed in the off-gas from the experiments performed in a bed of iron oxide: all CO produced during the gasification of the char was immediately oxidised by the oxygen carrier. In all the experiments in Fig. 7, the maximum rate of reaction occurred consistently at about $t \sim 200$–400 s. The corresponding conversion, X, at this time was ~0.2. Fig. 7 suggests that at low temperatures, i.e. 1073 K, the rate of gasification when the reaction was performed in sand is very similar to that performed in a bed of iron oxide: only a slight increase in the maximum rate was found (at $t \sim 200$–400 s). The time to reach 80% carbon conversion was about 17% lower in a bed of Fe_2O_3 than in a bed of sand at 1073 K.

Fig. 7 shows that at higher temperatures, i.e. 1123 and 1173 K, R'_g in a bed of oxygen carrier was considerably higher than in a bed of sand, particularly during the first *ca.* 240 s of the reaction, where $X \leqslant 0.3$–0.4. Table 3 shows the average time to reach 50%, 80% and 95% conversion ($t_{X=0.5}$, $t_{X=0.8}$, $t_{X=0.95}$, respectively). In general, the conversion times were decreased by increasing the temperature.

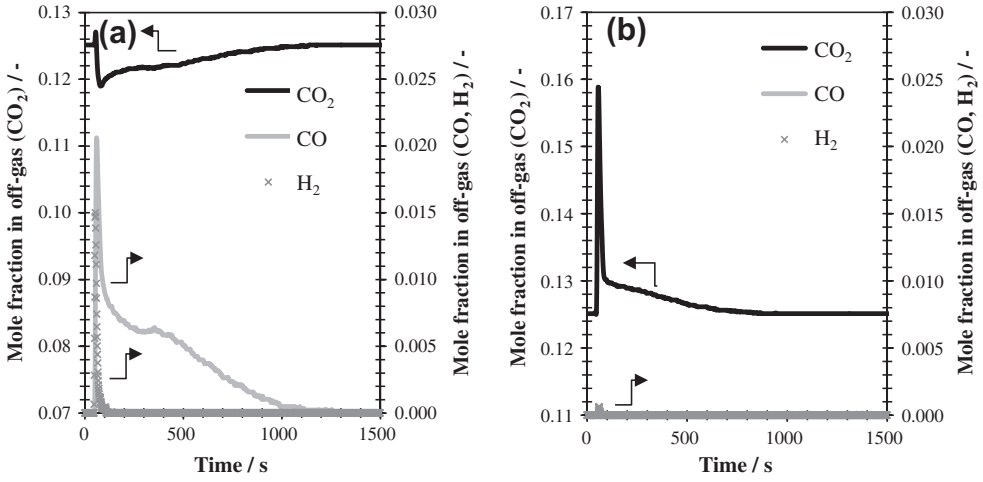

Fig. 6. Mole fractions in the off-gas during the gasification of Hambach lignite, $m_{batch} \sim 0.15$ g, d_p = +710, −1000 μm, in 12.5 mol.% CO_2, balance N_2, at 1073 K in a bed of (a) pure silica sand and (b) Fe_2O_3. Total volumetric flow rate is 50 $cm^3\ s^{-1}$ (as measured at 293 K and 1 bar).

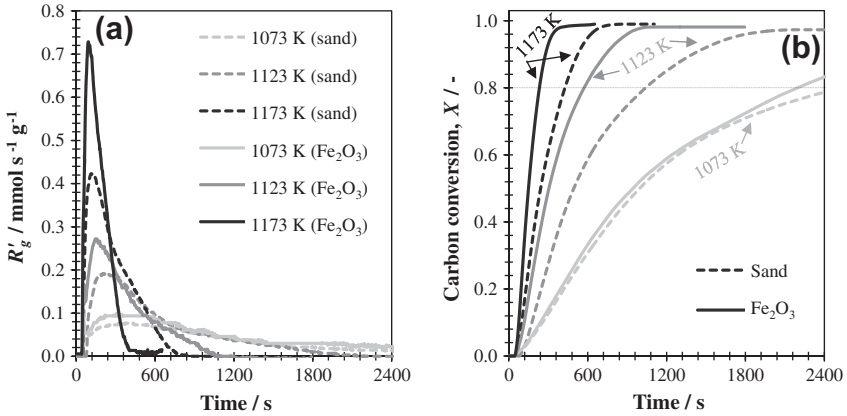

Fig. 7. Gasification of Hambach lignite char, $m_{batch} \sim 0.15$ g, d_p = +600, −1000 μm, in 12.5 mol.% CO_2, balance N_2, at 1073, 1123 and 1173 K in a bed of (---) pure silica sand and (—) Fe_2O_3. (a) Rate of production of CO (or equivalent rate for the experiments in Fe_2O_3) over time and (b) carbon conversion (N.B. the dotted horizontal line represents the 80% carbon conversion).

Table 3
Time (±20 s) to reach 50%, 80% and 95% carbon conversion, X, for the gasification of Hambach lignite char, d_p = +600, −1000 μm, in 12.5 mol.% CO_2, balance N_2, at 1073, 1123 and 1173 K in a bed of (i) silica sand and (ii) Fe_2O_3. Each experiment was repeated at least 3 times.

X	Silica sand			Fe_2O_3		
	1073 K	1123 K	1173 K	1073 K	1123 K	1173 K
Time in seconds (±20 s)						
50%	995	480	240	915	300	150
80%	2520	980	420	2080	550	230
95%	>3710	1525	585	3180	910	355

Table 3 shows that at 1073 K, the value of $t_{X=0.8}$ when char was gasified in a bed of Fe_2O_3 was only slightly smaller than when the char was gasified in a bed of sand. However, at both 1123 and 1173 K, $t_{X=0.8}$ was about 45% lower in a bed of Fe_2O_3 than in a bed of sand. For experiments performed at the same temperature, the times to reach a given conversion for the batch of char were consistently shorter when Fe_2O_3 was used as the bed material instead of sand, with a more significant difference as the temperature was increased.

Fig. 8 shows the results for the gasification of Hambach lignite coal under the same conditions as the lignite char. For the experiments in a bed of Fe_2O_3, there was little CO observed during the devolatilisation of the coal, i.e. a maximum peak concentration of ~500 ppm for all three temperatures. However, the concentration of CO dropped to zero within the first ~30–40 s, corresponding to the end of devolatilisation. This indicates that all CO produced after the devolatisation step subsequently reacted with the iron oxide. At 1073 K, the concentration of CO_2 observed during the devolatilisation step was considerably higher in the experiment with Fe_2O_3, due to the oxidation of CO and other volatiles by the oxygen carrier. However, after *ca.* 40 s it levelled off at a rate similar to that in a bed of sand. At higher temperatures, i.e. 1123 and 1173 K, the maximum value of R'_g is about 3.5–4.0 times higher in experiments in Fe_2O_3 than in a bed of sand. After the devolatilisation stage, R'_g still remains about 1.3–1.7 times higher than at the same time with the sand, during the first 60–120 s of char gasification. The time to reach 80% conversion at 1123 and 1173 K is reduced by the iron oxide by about 115 and 75 s, over that in sand, as shown in Table 4, corresponding to a reduction of about 44% and 47%, respectively.

4.5. Mass transfer limitation regime

Fig. 9 shows the rate of gasification as a function of time for a lignite char of two particle sizes for T = 1073 K and T = 1173 K. Ta-

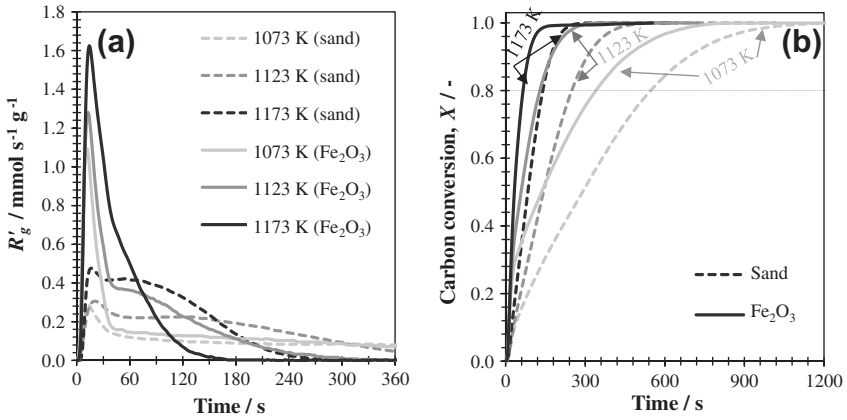

Fig. 8. Gasification of Hambach lignite coal, $m_{batch} \sim 0.15$ g, d_p = +710, −1000 μm, in 12.5 mol.% CO_2, balance N_2, at 1073, 1123 and 1173 K in a bed of (---) pure silica sand and (—) Fe_2O_3. (a) Rate of production of CO (or equivalent rate for the experiments in Fe_2O_3) over time and (b) carbon conversion (N.B. the dotted horizontal line represents the 80% carbon conversion).

Table 4
Time in seconds (±20 s) to reach 50%, 80% and 95% carbon conversion for the gasification of Hambach lignite coal, d_p = +710, −1000 μm, in 12.5 mol.% CO_2, balance N_2, at 1073, 1123 and 1173 K in a bed of (i) silica sand and (ii) Fe_2O_3. Each experiment was repeated at least 3 times.

X (−)	Silica sand			Fe_2O_3		
	1073 K	1123 K	1173 K	1073 K	1123 K	1173 K
Time in seconds (±20 s)						
50%	310	160	100	150	75	50
80%	565	265	160	360	150	85
95%	820	370	210	570	225	120

Table 5
Initial rates of formation of CO for the gasification of lignite char in a bed of sand in 12.5 mol% CO_2, balance N_2, using different particle sizes at T = 1073, 1123 and 1173 K.

Particle diameter (μm)	$R'_{g,0}$/mmol $s^{-1}g^{-1}$		
	1073 K	1123 K	1173 K
d_p = 800	0.054	0.103	0.300
d_p = 1200	0.053	0.094	0.236
d_p = 1550	0.053	0.093	0.202
d_p = 2130	0.052	0.093	0.214

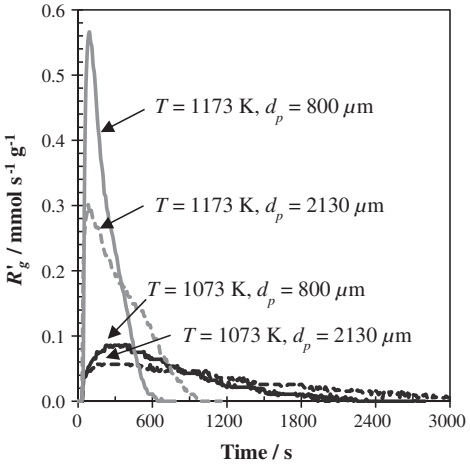

Fig. 9. Rate of production of CO per unit mass of carbon for the gasification of Hambach lignite char in sand in 12.5 mol.% CO_2, balance N_2, at 1073 and 1173 K for mean particle diameter, d_p = 800 and 2130 μm.

ble 5 shows the initial rates of formation of CO for the gasification of lignite char in a bed of sand using different particle mean diameters, ranging from 800 to 2130 μm, at various temperatures. The initial rates reflect similar trends to the burnout curves. A maximum rate was observed typically at conversions around X = 0.20. At 1073 K, there are minimal differences between the transient profiles of the rates of gasification, as shown in Fig. 9. This is in agreement with previous studies [28] where mass transfer limitations were found to be minimal at 1073 K. However, at a higher temperature of 1173 K, significant differences were observed in the rate of gasification for different particle sizes, both in the initial rate of formation of CO and in the transient rate profile. Of course, at this point it is not possible to say whether internal or external mass transfer is being altered in these experiments.

5. Discussion

5.1. The intrinsic kinetics of gasification of lignite char

The oxygen carrier affects the local concentrations of CO and CO_2 around a char particle by reducing the concentration of the former and increasing the latter. Thus, the intrinsic rate of reaction, as given by Eq. (6), increases. The inhibitory effect of CO decreases with temperature, as shown in Eq. (7), because of the negative activation energy E_{k_{-1}/k_1} [52]. However, Eq. (6) is only concerned with the reaction of a surface of carbon, freely exposed to the reactant gas. The reaction kinetics, in practice, are complicated by the development of the pore network in a particle as the gasification proceeds. In the experiments conducted here, it can be seen that there is an increase in rate of reaction with conversion up to a value of ~0.20, attributable to (i) increased surface area from pore enlargement by reaction and (ii) increased porosity for gases entering and leaving the particle. Beyond this conversion, the rate of reaction falls, probably because the net internal surface area decreases as the pores enlarge.

Because the structure of a fuel particle will change with conversion, the following discussion is concerned with the *initial* rate of gasification of lignite *char*, since the initial morphological properties of char were known. To determine the values $2ck_2$, k_2/k_1 and k_{-1}/k_1 in Eq. (6), the initial rates of gasification in sand of lignite char, d_p = 600–1000 μm, were obtained from experiments conducted from 1048 K to 1248 K for a range of mole fractions of CO_2, from 0.11 to 0.85, balance N_2 and, in some particular cases, CO. Assuming the rate of gasification obeys Eq. (6), and neglecting the term $p^2_{CO,s}/K_p$, a plot of $[(k_{-1}/k_1)p_{CO,s} + p_{CO_2,s}]$ against $p_{CO_2,s}/R'_{g,0}$

Table 6
Kinetic parameters derived from the experimental results from 1073 to 1248 K with Hambach lignite char, d_p = 600–1000 μm. The predicted initial rates using these kinetic parameters have an average total deviation of 1 ± 5% with respect to the observed experimental initial rates. K_p is consistent with partial pressures expressed in bar.

T (K)	1048	1073	1098	1123	1173	1223	1248
K_p (–)	3.8	6.3	9.3	12.6	35.8	79.4	100.0
E_{k_{-1}/k_1} (kJ mol^{-1}) (±2.0)	−91.0	−91.0	−91.0	−91.0	−91.0	−91.0	−91.0
k_{-1}/k_1 (–)	8.27	6.48	5.14	4.12	2.72	1.86	1.55
$2ck_2$ (mmol s^{-1} g^{-1})	0.082	0.114	0.229	0.622	3.065	2.877	3.420
$2ck_1$ (mmol s^{-1} g^{-1} bar^{-1})	0.361	0.553	1.108	0.857	3.911	13.469	17.125
k_2/k_1 (bar)	0.23	0.21	0.21	0.73	0.78	0.21	0.20

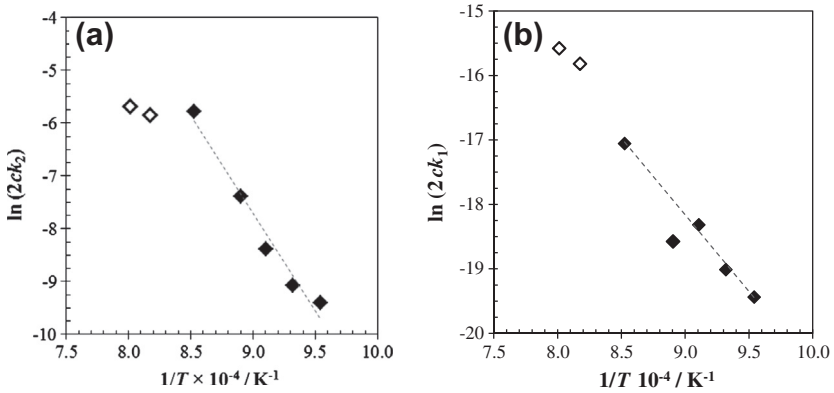

Fig. 10. Plots of (a) $\ln(2ck_2)$ against $1/T$ and (b) $\ln(2ck_1)$ against $1/T$: (◇) T = 1223–1248 K and (♦) T = 1048–1173 K. The straight lines are based on T = 1048–1173 K, illustrated by the closed symbols.

should give a straight line of slope $1/2ck_2$ and intercept $1/2ck_1$. The term k_{-1}/k_1 was obtained from Eq. (7) and with a value E_{k_{-1}/k_1} (found by best fit to the experiments) of −91 kJ mol^{-1}, in good agreement with previously-reported values [5,22,38]. A more detailed description of these calculations and the implications of neglecting $p^2_{CO,s}/K_p$ are explored in the Appendix. The estimated kinetic parameters from Eq. (6), derived from the experimental results between 1073 and 1248 K, are shown in Table 6. The average total deviation between the initial observed rates experimentally and the rate evaluated using the estimated parameters in Eq. (6), is 1.1 ± 5.3%.

Fig. 10 shows two regimes; above ~1173 K, there is a change in the activation energy of $2ck_2$, suggesting the onset of mass transfer limitations. This is in line with the observation in Section 4.5, where the observed rate of reaction decreased significantly with different particle sizes at T = 1173 K. Assuming $2ck_2$ and $2ck_1$ obey an Arrhenius relationship, the resulting values of the pre-exponential factors and activation energies $A_{2ck_2}, A_{2ck_1}, E_{2ck_2}, E_{2ck_1}$ and the corresponding parameters from Eq. (7), A_{k_{-1}/k_1} and E_{k_{-1}/k_1} are shown in Table 7. The regression was performed only for results from temperatures at, or below, 1173 K, illustrated by the closed symbols in Fig. 10.

5.2. Solution of the mass transfer models of Sections 2.2 and 2.3 coupled to the intrinsic kinetics

In order to account for both mass transfer effects within the particle and in the boundary layer surrounding it, the equations outlined in Sections 2.2 and 2.3 were solved simultaneously.

Table 8 summarises the assumed properties of the particle of char used in this study, which were used in the solution of the intraparticle mass transfer model, outlined in Section 2.2. It should be noted that, in reality, the internal structure of the porous particle of char is made up of a distribution of pore sizes. However, for this analysis, a mean pore radius was used. The initial pore radius, i.e. at X = 0, was chosen to ensure that the model reproduced the observed initial rate of reaction at 1173 K for the different particle sizes given in Table 5. The assumed value of mean pore radius of 50 nm was close to the value determined by N_2 adsorption analysis. The porosity and density of the char were determined by mercury intrusion porosimetry. The value of the tortuosity factor was assumed to be the reciprocal of porosity, as suggested by [53]. The estimated value of the tortuosity factor was found to be within the typical range of values used in studies of porous catalysts (e.g. [54,55]).

In order to account for the evolution of the pore structure as conversion increases, the porosity at a particular conversion, $\varepsilon(X)$, is given by

$$\varepsilon(X) = \varepsilon_0 + (1 - \varepsilon_0)X \tag{35}$$

For the initial phase of the reaction where the rate of gasification increases with X, *viz.* $0 < X < 0.2$, the evolution of the mean pore radius was approximated to be proportional to the increase in surface area, i.e.

$$R_{pore}(X) = R_{pore,0} \times f(X) \tag{36}$$

In this study, given minimal mass transfer limitations at T = 1073 K, the ratio of the rate of reaction at a particular conversion to the initial rate of reaction reflects, generally, the variation in the surface area available for reaction as the reaction proceeds in the absence of intraparticle gradients in gas concentration. The value of $f(X)$ was found by matching an arbitrary function to the experimental results at 1073 K, as illustrated in Fig. 11: the variation of the surface area at higher temperatures was assumed to follow this function. In general, $f(X)$ increases to a maximum and then decreases as the pores begin to overlap. Here, for the sake for simplicity, for $X > 0.2$, the pore size was maintained at R_{pore} (X = 0.2). In principle, the pore size should continue to increase as conversion increases.

Table 7
Values of parameters for the temperature dependence of the intrinsic parameters for the gasification of char with CO_2.

A_{2ck_2}/mol $s^{-1}g^{-1}$	E_{2ck_2}/kJ mol^{-1}	A_{2ck_1}/mol $s^{-1}g^{-1}$ bar^{-1}	E_{2ck_1}/kJ mol^{-1}	A_{k_{-1}/k_1}/–	E_{k_{-1}/k_1}/kJ mol^{-1}
$1.26 \pm 0.1 \times 10^{11}$	290 ± 20	$2.56 \pm 0.2 \times 10^{6}$	200 ± 20	$2.4 \pm 0.2 \times 10^{-4}$	−91 ± 2

Table 8
Assumed properties of the particle of char for the intraparticle model.

Property	Value
Initial porosity, ε_0	0.5
Tortuosity, τ^2	2
Mean pore radius, $R_{pore,0}$	50 nm
Density of the particle of char, ρ_e	800,000 g m^{-3}
Radius of the spherical particle of char, R_p	400 μm

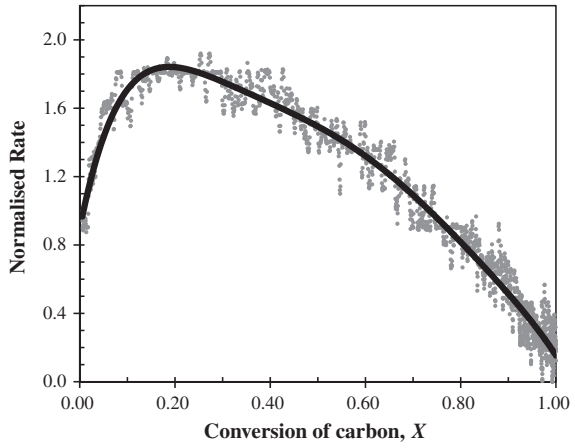

Fig. 11. Normalised rate of gasification as a function of conversion, X, for gasification in a bed of sand at $T = 1073$ K and with $y_{CO_2,bulk} = 0.125$ balance N_2. The solid line was fitted to the experimental points.

However, at large pore sizes, the effective diffusivity is only mildly dependent on the pore size because only Knudsen diffusivity is a function of pore size whereas bulk diffusivity is independent of the pore size. The increase in the overall diffusivity within the particle is also reflected by the increase in the voidage, already accounted for by Eq. (35).

An important parameter in the solution of the mass transfer equations surrounding the particle, namely Eqs. (22) and (24)–(26), is the thickness of the boundary layer, δ, surrounding the spherical particle of char. This parameter was determined using the following expression [56]:

$$Sh = Sh_0\left(1 + \frac{d_p}{2\delta}\right) \tag{37}$$

where Sh_0 is the Sherwood number for the stagnant case, given for a fluidised bed by $Sh_0 = 2\varepsilon_{mf}$. The correlations to obtain Sh and all other necessary parameters are explained in [5]. Table 9 shows the value of the parameters used for the estimation of δ at two different temperatures, i.e. 1073 and 1173 K, for experiments involving the gasification of lignite char, $d_p = 800$ μm, in a bed of sand. The value of δ is about 6.4×10^{-4} and 6.0×10^{-4} m, respectively.

In order to solve the model describing the mass transfer in the boundary layer surrounding the particle of char, described by Eqs. (22)–(26) in Section 2.3, an estimate of the flux of CO at the surface of the particle, $J_{1,s}$, is required. In the presence of internal mass transfer limitations, the solution of the equations described in Section 2.2, i.e. Eqs. (9)–(14), is required in order to obtain an estimate of $J_{1,s}$. The equations describing mass transfer within the particle

Table 9
Parameters used for the determination of δ. Example for gasification of particles of lignite char, $d_p = 800$ μm, in sand, at 1073 and 1176 K.

Parameter	$T = 1073$ K	$T = 1173$ K	Units
H_{mf}	0.029	0.029	m
U	0.268	0.293	m s^{-1}
U_{mf}	0.050	0.047	m s^{-1}
ε_b	0.500	0.520	–
U_B	0.436	0.473	m s^{-1}
$d_{b,m}$	0.010	0.010	m
U_p	0.146	0.197	m s^{-1}
υ	1.30×10^{-4}	1.50×10^{-4}	m^2 s^{-1}
D_m	1.54×10^{-4}	1.80×10^{-4}	m^2 s^{-1}
d_p	8.0×10^{-4}	8.0×10^{-4}	m
Sh	1.427	1.467	–
δ	6.43×10^{-4}	6.00×10^{-4}	m
$R_p + \delta$	1.04×10^{-3}	1.00×10^{-3}	m
$(R_p + \delta)/R_p$	2.608	2.500	

require an estimate of the composition of the mixture at the surface of the particle, which is a function of the external mass transfer. An iterative scheme was developed in order to solve these equations simultaneously. Using an initial guess for $J_{1,s}$, the ODEs describing the mass transfer outside the particle (Eqs. (22), (24)–(26)) were solved using the MATLAB solver *bvp4c*, with the boundary conditions given by Eqs. (28) and (29), to give the profile of the composition within the boundary layer from $r = R_p$ to $r = R_p + \delta$. The composition of the mixture at the surface of the particle, i.e. at $r = R_p$, from this initial profile was used as an estimate for the solution of the intraparticle mass transfer model, described by Eqs. (9) and (11)–(14) (again using *bvp4c*). The solution of the model for intraparticle mass transfer provides the spatial profiles of fluxes, composition and total pressure within the char particle, bounded by $r = 0$ and $r = R_p$, producing a revised estimate for $J_{1,s}$. This new value of $J_{1,s}$ was then used in the solution of the external mass transfer model. This process was iterated until the values of $J_{1,s}$ converged to within 0.02% of the converged value of $J_{1,s}$.

It should be noted that in the external boundary layer, with non-equi-mass diffusion, a pressure gradient equal to $dP/dr = -ku$ (where u is the mass average velocity and k is the permeability of the bed) is required to ensure conservation of momentum; however, in all experiments presented in this paper, the permeability of the bed is large, and pressure gradients small compared to the absolute pressure and that required to ensure fluidisation. For instance, from Fig. 7, at 1173 K and $X = 0.20$, the mass average velocity from the particle surface, u, was about 0.0016 m s^{-1}, much lower than the interstitial velocity, U_{mf}/ε_{mf} of ~0.11 m s^{-1}. This indicates that there was no tendency to form voids or bubbles around the reacting particle. Thus, pressure variations can be neglected in this model, and the pressure is taken to be constant.

The overall rate of conversion of the char particle to CO *via* gasification can then be obtained either by integration of the local rates of gasification over the interior of the particle, i.e.

$$R'_{overall,CO} = \int_{r=0}^{r=R} R' \times 4\pi r^2 dr \tag{38}$$

where R' is the local rate of reaction at radius r, or from the flux of CO at $r = R_p$ by

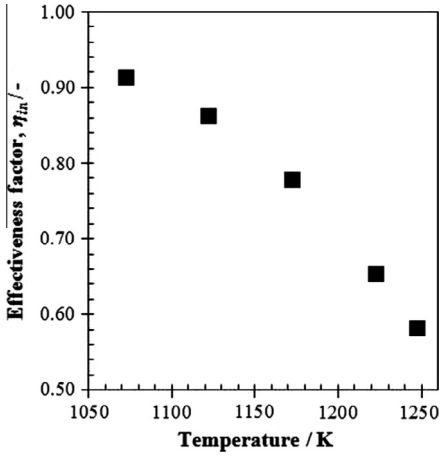

Fig. 12. Calculated effectiveness factor as a function of temperature for $y_{2,bulk} = 0.125$ and $y_{3,bulk} = 0.875$ at $X = 0$. In this case, the particle of char was fluidised in sand.

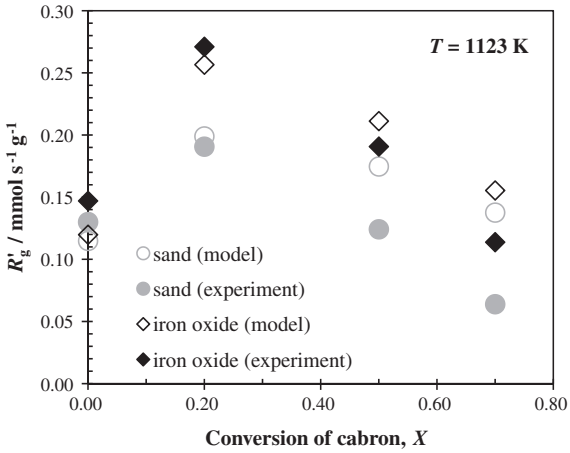

Fig. 14. Rate of gasification for different conversions at 1123 K when lignite char, $d_p = 800$ μm, was gasified in sand or in iron oxide.

$$R'_{overall,CO} = \frac{3J_{1,s}}{R_p \rho_e}. \quad (39)$$

Fig. 12 presents an assessment of the extent of mass transfer limitations within the particle of char as a function of temperature. Here, the effectiveness factor, η_{in}, is defined as the ratio between the overall rate of reaction and the rate of gasification if no mass transfer limitations were present within the particle, thus

$$\eta_{in} = \frac{R'_{overall,CO}}{R'_g(y_{1,s}, y_{2,s})} \quad (40)$$

where $R'_g(y_{1,s}, y_{2,s})$ is the intrinsic rate defined by Eq. (6) evaluated using the composition at the surface of the particle, after accounting for the variation of composition within the boundary layer surrounding the particle. Fig. 12 shows that the effect of internal mass transfer becomes increasingly significant at temperatures above 1173 K. In general, this is in line with the experimental results outlined in Table 5, where larger variations in the observed initial rate of gasification were observed at higher temperatures.

5.3. Effect of looping agent on the rate of gasification of char

Fig. 7 illustrates the effect of iron oxide on the rate of gasification. There is an enhancement in the rate of gasification when Fe_2O_3 is present which is more pronounced at higher temperatures (i.e. 1123 and 1173 K). It was also found that, in general, there was only a small difference between the observed initial rates of gasification in either sand or in Fe_2O_3, *viz.* when $X = 0$. However, as the reaction proceeds, the rate of gasification of char in Fe_2O_3 became much larger compared to that in sand, especially at $X \approx 0.2$. This can be seen by comparing the experimental rates at $X = 0$ and $X = 0.2$ in Figs. 14 and 15. Other studies (not shown here for simplicity) showed that there was no difference between the measured rates in a bed of sand and in a bed of reduced Fe_2O_3 to Fe_3O_4 at the temperatures studied, i.e. 1073, 1123 and 1173 K. This led to the conclusion that any potential catalytic effect of reduced Fe_2O_3 (i.e. as Fe_3O_4) on the gasification of char could be neglected in this study.

The solution of the mass transfer model coupled with the intrinsic kinetics of the gasification of char could be used to explain the observed effect of Fe_2O_3 on the rate of gasification. Fig. 13 shows the profile of the composition of CO and CO_2 as a function of the dimensionless radius, $\sigma_r = r/R_p$, in a particle of char with a particle diameter of 800 μm, at $T = 1173$ K and $X = 0$ and $X = 0.2$. It can be seen that the presence of Fe_2O_3 decreases the presence of CO throughout the entire particle where $0 < \sigma_r < 1$. Since CO has an inhibiting effect on the rate of gasification, as expressed by the rate expression in Eq. (6), a reduction in the partial pressure of CO increases the observed rate of gasification. Furthermore, since Fe_2O_3 consumes CO to produce CO_2 by Reaction (2), its presence also maintains a higher partial pressure of CO_2 at the surface of

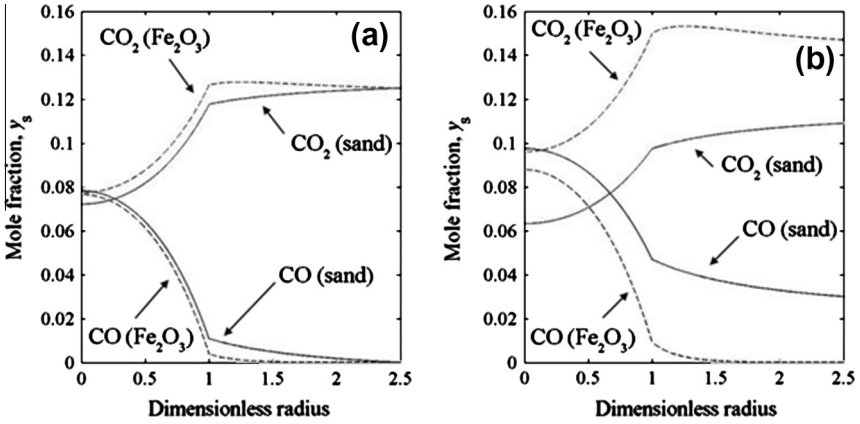

Fig. 13. Comparison of the profiles of composition of CO and CO_2 from $r = 0$ to $r = R_p + \delta$ when the particles of char, $d_p = 800$ μm, were fluidised with sand and Fe_2O_3. $T = 1173$ K and (a) $X = 0$ and (b) $X = 0.2$.

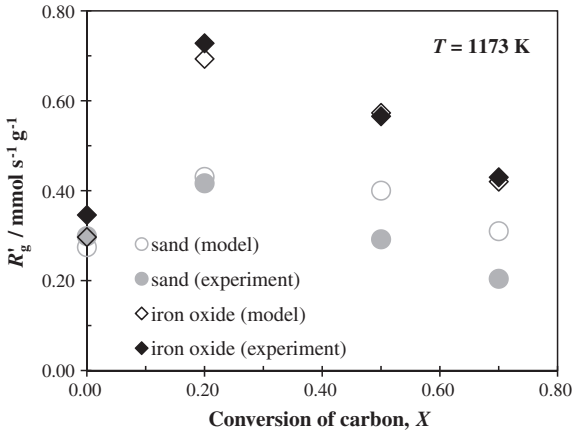

Fig. 15. Rate of gasification for different conversions at 1173 K when lignite char, d_p = 800 μm, was gasified in sand or in iron oxide.

the particle and within the particle. These effects on the partial pressures of CO and CO_2 are more significant at higher conversions, e.g. at X = 0.2, as shown in Fig. 13(b). It should be noted that this effect is significant because re-oxidation of CO to CO_2 by carrier is much faster than the reaction of CO_2 with char. An examination of the domain from σ_r = 1 to σ_r = 2.5, *viz.* external to the particle of char in Fig. 13, reveals a maximum in the mole fraction of CO_2. Since the rate of consumption of CO by Reaction (2) is very fast, a region of positive (outward) flux of CO_2 at around σ_r = 1.25–2.5 occurs and results in the occurrence of the maximum in the mole fraction of CO_2. In the absence of Fe_2O_3, this is not possible as there is no source of oxidation of CO to CO_2 and the flux of CO_2 is accordingly negative throughout the entire domain.

However, as shown in Fig. 13(a), at X = 0, the reaction is largely limited by intraparticle diffusion. CO is only oxidised to CO_2 by Fe_2O_3 when σ_r > 1, hence, the overall effect of Fe_2O_3 on the overall rate is relatively small during the initial phase of the reaction. As the reaction proceeds and conversion increases (Fig. 13(b)), an increase in porosity and the pore size is expected, accounted for by Eqs. (35) and (36). Furthermore, there is also an increase in the overall activity of gasification as the surface area increases from X = 0 to X = 0.2, which is reflected by $f(X)$ which was derived from Fig. 11. In general, this increase in rate leads to the accumulation of more CO at the surface of the particle. Hence, in the presence of Fe_2O_3, the rate of reaction would be much faster than that in sand. Additionally, at X = 0.2, the model was solved with a characteristic pore radius of 94 nm and a porosity of 0.6, leading to an increase in the internal effectiveness, i.e. the particle is less limited by internal mass transfer than at X = 0. The increase in the effective diffusivity of gases within the particle and the overall activity of the particle due to the increase in the surface area available for reaction means that there is a large difference between the amount of CO accumulated at the surface of the particle, depending on whether it was gasified in sand or Fe_2O_3. As before, this effect is prominent at high temperatures of 1123 K and 1173 K and can be seen by comparing the rates at X = 0.2 in Figs. 14 and 15. There is excellent agreement between rates observed experimentally and those predicted by the model, especially at X = 0 and X = 0.2. It should be noted that the effect of the iron oxide conversion on the rate as suggested by [46] has been ignored in this work, since the carrier is in excess and each experiment starts with fully oxidised bed.

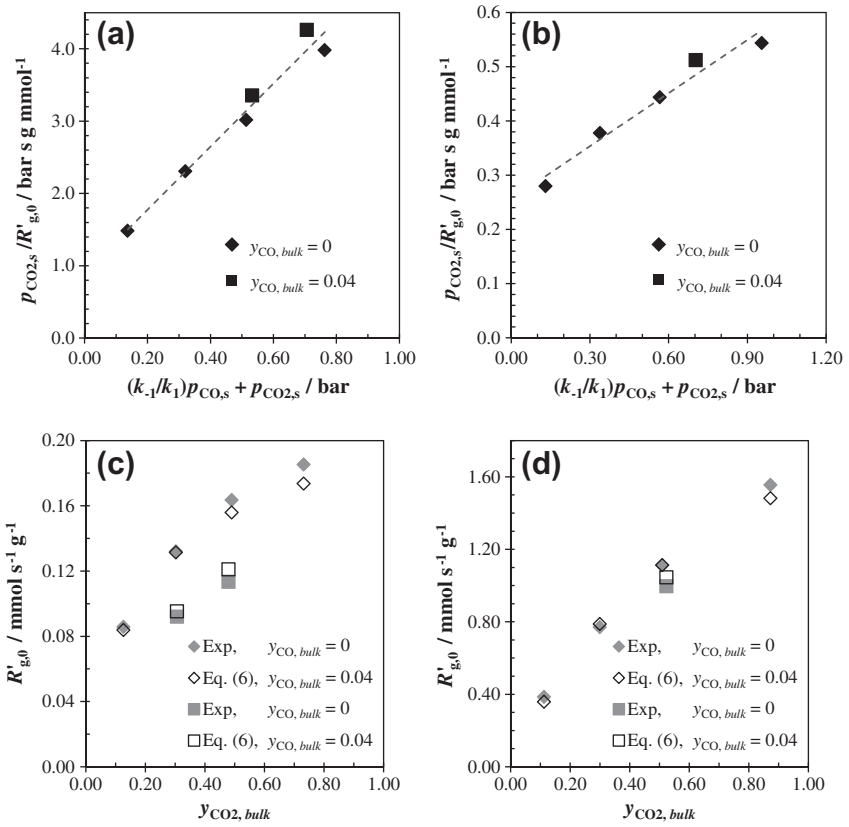

Fig. A.1. Gasification of batches of lignite char, d_p = 600–1000 μm, at various concentrations of CO_2 and CO. at (a and c) 1098 K and (b and d) 1173 K. Regression line of figures (a) and (b) was calculated using Eq. (A.1) with $y_{CO,bulk}$ = 0 (♦) and $y_{CO,bulk}$ = 0.04 (■). Figures (c) and (d) compare the initial rates of reaction observed experimentally with $y_{CO,bulk}$ = 0.0 (♦) and $y_{CO,bulk}$ = 0.04 (◇) and the rates using the estimated kinetic parameters from Eq. (6) with $y_{CO,bulk}$ = 0.0 (■) and $y_{CO,bulk}$ = 0.04 (□).

The model also predicts a convergence in the rate of reactions in sand and Fe_2O_3 in the later stages of the reaction, e.g. at $X = 0.5$ and 0.7. Under such conditions, the surface area decreases owing to overlapping of pores and the overall activity decreases. When the char was gasified in sand, less CO accumulated at the surface, decreasing the observed effect of Fe_2O_3 on the overall rate. As noted in Section 2.2, a major limitation of the current model is that average conversions were used and assumed to be uniform across the particle. This is justifiable during the initial stage of the reaction. However, the effect on the rate of reaction of a particle of char with a spatial distribution of conversion, compared to the assumed uniform one, is expected to be more prominent in the later stages of the reaction. Other complications involving the breaking up of particles at high conversions were also not accounted for in the current model.

The models presented in this study are independent of the relative loading of char and Fe_2O_3 since the char is sufficiently dilute to ensure that the boundary layer around a particle of char only contains iron oxide. At high loadings of carbon, this assumption would break down. A key variable affecting when the loading of Fe_2O_3 becomes significant is the activity of the iron oxide, in particular the rate at which it is able to destroy carbon monoxide compared to the rate at which the carbon monoxide can diffuse out of the boundary layer. If the particles of Fe_2O_3 have a low reactivity, where k_l is low, there would be no enhancement in mass transfer. In this study, the iron oxide carrier is sufficiently reactive at the temperatures used to ensure that the carbon monoxide does react in the boundary layer.

It should also be noted that since the rate of gasification is slow at 1073 K, only a very small amount of CO accumulates at the surface of the particle. Under such conditions, the effect of internal mass transfer is also negligible as shown by the results in Table 5. The presence of Fe_2O_3 provides negligible enhancement at such a condition because effect of the removal of CO by Fe_2O_3 would be minimal.

6. Conclusions

Batch gasification by CO_2 in a fluidised bed was undertaken at different temperatures using a lignite as fuel. The lignite and its char were found to be very reactive, even at 1073 K, making it a promising type of solid fuel for use in CLC. Furthermore, experimental results showed an enhancement of the apparent rate of gasification of lignite when Fe_2O_3 was present in the fluidising bed, especially at temperatures above 1123 K. Such conditions corresponded to the point at which mass transfer limitations within and surrounding the particle became significant, and suggested that the Fe_2O_3 was influencing mass transfer and hence the overall rate of gasification.

A mathematical model coupling the intrinsic kinetics of the gasification of lignite char with the mass transfer limitations within and surrounding the particle of char, and accounting for the evolution of porosity in the char, was developed; there was excellent agreement between the modelled and observed rates of gasification. Under conditions where mass transfer limitations were negligible, e.g. at $T = 1073$ K, the intrinsic kinetics was described well by the modified Ergun equation, where CO has an inhibitory effect on the rate of gasification, and the effect of Fe_2O_3 was small. When char was gasified in sand at $T \geqslant 1123$ K, external mass transfer began to limit the rate significantly, with the fast rate of reaction causing a significant build-up of CO at the surface of the particle. At conversions of $X \approx 0.2$, the surface area available for reaction is at its maximum, leading to a significant increase in the observed rate. A particle of char at $X = 0.2$ experiences less mass transfer resistance within the particle compared to its initial conditions. When this factor is coupled with the increased surface area, there results a larger build-up of CO at the surface of the particle than is present at the start of the reaction. Hence, the ability of Fe_2O_3 to remove CO from the surface of the particle leads to a significant difference between the rates of gasification in sand and Fe_2O_3, particularly when $X \approx 0.2$. Thus, when external mass transfer begins to affect the rate, conversion of the CO to CO_2 by the Fe_2O_3 in the boundary layer enhances the rate of removal of the inhibitory CO from the particle, whilst re-generating the reactant CO_2, effectively removing the limitation caused by external mass transfer.

Acknowledgements

The authors are grateful to the Engineering and Physical Sciences Research Council (Grant reference number: EP/G063265/1), the CONACYT and the Cambridge International Scholarship Scheme Trust for financial support.

Appendix A. Estimation of the kinetic parameters in Eq. (6)

The kinetic parameters in Eq. (6) were derived from experimental results between 1048 and 1248 K. Since the term $PCO^2, s/K_p$ in the numerator of Eq. (6) was small in these experiments, it was neglected, thereby allowing Eq. (6) to be rearranged as

$$\frac{p_{CO_2,s}}{R'_{g,0}} = \frac{1}{2ck_2}[(k_{-1}/k_1)p_{CO,s} + p_{CO_2,s}] + \frac{1}{2ck_1} \quad (A.1)$$

where $p_{CO,s}$ and $p_{CO_2,s}$ are the mole fractions of CO and CO_2 at the surface of the particle, respectively, and $R'_{g,0}$ is the initial rate of reaction observed in the experiments. The implications of neglecting $PCO^2, s/K_p$ are explored later. The term k_{-1}/k_1 was obtained from Eq. (7), with the activation energy, E_{k_{-1}/k_1}, optimised by varying k_{-1}/k_1 until the fit given by (A.1) had the highest correlation coefficient with the observed rates. The straight lines shown in Fig. A.1(a) and (b) illustrate that the rate of gasification could be described by Eq. (6). All experiments at the different temperatures were fitted to within ±5%. The corresponding values of the slope and intercept of the straight line plots were used to calculate $2ck_1$ and $2ck_2$. Fig. A.1(c) and (d) show the agreement, at 1098 K and 1173 K, between the initial rates which were observed experimentally and those when the estimated kinetic parameters for Eq. (6) were used.

In order to be able to ignore $PCO^2, s/K_p$, this term should be much smaller than $p_{CO_2,s}$, typically between 0.11 and 0.86 bar. At low temperatures, say 1098 K, $K_p = 9.3$, consistent with partial pressures expressed in bar. At this temperature, no external mass transfer limitation is expected, hence $p_{CO,s} \approx p_{CO,bulk} \approx 0$ and $PCO^2, s/K_p \to 0$. The validity of neglecting the effect of external mass transfer at low temperatures, i.e. 1098 K, can be investigated roughly by determining the maximum rate of gasification if controlled solely by external mass transfer, R'_{max}. This is given by [56]:

$$R'_{max} = 2 \times 0.91 \times ShD_m[CO_2]_{bulk}\frac{6}{\rho_e d_p^2} \quad (A.2)$$

This estimate will be crude because it assumes equimolar counter diffusion. At 1098 K, D_m, the diffusivity of CO_2 in the gas mixture, is 1.70×10^{-4} m^2 s^{-1} and, with 12.5 mol.% CO_2, $[CO_2]_{bulk} = 1.4$ mol m^{-3}. It was shown in Table 9 that for a char particle of $d_p = 800$ μm, $Sh \approx 1.5$, so that $R'_{max} = 7.1$ mmol s^{-1}g^{-1}, which is much larger than the measured rate in Fig. A.1 of ~0.08 mmol s^{-1} g^{-1}. Thus, the rate of external mass transfer does not affect the measured kinetics at 1098 K. At higher temperatures, say 1173 K, external mass transfer is expected to be more significant with the lignite coal, therefore $p_{CO,s} > 0$. However, K_p at 1173 K is 35.8, much larger than any expected partial pressure of CO at the surface of the

particle, thus $PCO^2, s/K_p$ remains small. Of course, the error incurred by ignoring this term will be higher at larger values of $p_{CO,s}$. However, at 1173 K and $p_{CO,s} = 0.04$ bar, for example, the term $PCO^2, s/K_p$ takes a value of 4.5×10^{-5} bar, whilst $p_{CO_2,s}$ is at least 0.11 bar, much larger than the former term. The absolute error when calculating $R'_{g,0}$ at these conditions by ignoring $PCO^2, s/K_p$ is <0.1%. Thus, this term can be ignored in the estimation of the kinetic parameters described in Section 5.1.

References

[1] International Energy Agency. Key world energy statistics. Paris: OECD IEA; 2012.
[2] Enerdata, 2004: A global energy data base including OECD data. Grenoble, France; 2004.
[3] Lyngfelt A, Leckner B, Mattisson T. A fluidized bed combustion process with inherent CO_2 separation: application of chemical-looping combustion. Chem Eng Sci 2001;56:3101–13.
[4] Kronberger B, Lyngfelt A, Loffler G, Hofbauer H. Design and fluid dynamic analysis of a bench-scale combustion system with CO_2 separation – chemical looping combustion. Ind Eng Chem Res 2005;44:546–56.
[5] Dennis JS, Scott SA. In situ gasification of a lignite coal and CO_2 separation using chemical looping with a Cu-based oxygen carrier. Fuel 2010;89:1623–40.
[6] Bohn CD, Cleeton JP, Müller CR, Chuang SY, Scott SA, Dennis JS. Stabilizing iron oxide used in cycles of reduction and oxidation for hydrogen production. Energy Fuels 2010;24:4025–33.
[7] Kierzkowska AM, Bohn CD, Scott SA, Cleeton JP, Dennis JS, Müller CR. Development of iron oxide carriers for chemical looping combustion using sol–gel. Ind Eng Chem Res 2010;49:5383–91.
[8] Imtiaz Q, Kierzkowska AM, Broda M, Müller CR. Synthesis of Cu-rich, Al_2O_3-stabilized oxygen carriers using a coprecipitation technique: redox and carbon formation characteristics. Environ Sci Technol 2012;46:3561–6.
[9] Adánez J, Cuadrat A, Abad A, Gayán P, de Diego LF, García-Labiano F. Ilmenite activation during consecutive redox cycles in chemical-looping combustion. Energy Fuels 2010;24:1402–13.
[10] Lyngfelt A, Kronberger B, Adanez J, Morin JX, Hurst P. The grace project development of oxygen carrier particles for chemical looping combustion. Design resented at the seventh international conference on greenhouse gas control. Canada: Vancouver; 2004.
[11] de Diego LF, Garcia-Labiano F, Gayan P, Celaya J, Palacios JM, Adanez J. Operation of a 10 kWth chemical looping combustor during 200 h with a CuO–Al_2O_3 oxygen carrier. Fuel 2007;86:1036–45.
[12] Ishida M, Zheng D, Akehata T. Evaluation of a chemical-looping-combustion power-generation system by graphic exergy analysis. Energy 1987;12:147–54.
[13] Wolf J, Anheden M, Yan J. Comparison of nickel- and iron-based oxygen carriers in chemical looping combustion for CO_2 capture in power generation. Fuel 2005;84:993–1006.
[14] Kvamsdal HM, Jordal K, Bolland O. A quantitative comparison of gas turbine cycles with CO_2 capture. Energy 2007;32:10–24.
[15] McGlashan NR. Chemical-looping combustion – a thermodynamic study. Proc I Mech E Part C 2008;222:1005–19.
[16] Ishida M, Jin H. A novel combustor based on chemical looping reactions and its reaction kinetics. J Chem Eng Jpn 1994;27:296–302.
[17] Adanez J, Gayan P, Celaya J, de Diego LF, Garcia-Labiano F, Abad A. Chemical looping combustion in a 10 kWth prototype using a CuO/Al_2O_3 oxygen carrier: effect of operating conditions on methane combustion. Ind Eng Chem Res 2006;45:6075–80.
[18] Lyon RK, Cole JA. Unmixed combustion: an alternative to fire. Combust Flame 2000;121:249–61.
[19] Cao Y, Liu K, Riley JT, Pan WP. Application of a circulating fluidized bed process for the chemical looping combustion of solid fuels. Preprints of symposia – American Chemical Society. Div Fuel Chem 2004;49:815–6.
[20] Cao Y, Pan WP. Investigation of chemical looping combustion by solid fuels. 1. Process analysis. Energy Fuels 2006;20:1836–44.
[21] Cao Y, Casenas B, Pan WP. Investigation of chemical looping by solid fuels. 2. Redox reaction kinetic and product characterization with coal, biomass, and solid waste as solid fuels and CuO as an oxygen carrier. Energy Fuels 2006;20:1845–54.
[22] Dennis JS, Scott SA, Hayhurst AN. In situ gasification of coal using steam with chemical looping: a technique for isolating CO_2 from burning a solid fuel. J Energy Inst 2006;79:187–90.
[23] Scott SA, Dennis JS, Hayhurst AN, Brown T. In situ gasification of a solid fuel and CO_2 separation using chemical looping. AIChE J 2006;52:3325–8.
[24] Leion H, Mattisson T, Lyngfelt A. The use of petroleum coke as fuel in chemical looping combustion. Fuel 2007;86:1947–58.
[25] Berguerand N, Lyngfelt A. Design and operation of a 10 kWth chemical-looping combustor for solid fuels – testing with South African coal. Fuel 2008;87:2713–26.
[26] Leion H, Mattisson T, Lyngfelt A. Solid fuels in chemical looping combustion. Int J Greenhouse Gas Control 2008;2:180–93.
[27] Song Q, Xiao R, Deng Z, Shen L, Xiao J, Zhang M. Effect of temperature on reduction of $CaSO_4$ oxygen carrier in chemical-looping combustion of a simulated flue gas in a fluidized bed reactor. Ind Eng Chem Res 2008;47:8148–59.
[28] Brown TA, Davidson JF, Hayhurst AN, Dennis JS, Scott SA. Chemical looping combustion of a lignite char under semi-batch conditions with an iron-based oxygen carrier. Energy Fuels 2010;24:3034–48.
[29] Linderholm C, Lyngfelt A, Cuadrat A, Jerndal E. Chemical-looping combustion of solid fuels – operation in a 10 kW unit with two fuels, above-bed and in-bed fuel feed and two oxygen carriers, manganese ore and ilmenite. Fuel 2012;102:808–22.
[30] Mendiara T, Gayán P, Abad A, de Diego LF, García-Labiano F, Adánez J. Performance of a bauxite waste as oxygen-carrier for chemical-looping combustion using coal as fuel. Fuel Process Technol 2013;109:57–69.
[31] Song T, Shen T, Shen L, Xiao J, Gu H, Zhang S. Evaluation of hematite oxygen carrier in chemical-looping combustion of coal. Fuel 2013;104:244–52.
[32] Cuadrat A, Abad A, García-Labiano F, Gayán P, de Diego LF, Adánez J. Relevance of the coal rank on the performance of the in situ gasification chemical-looping combustion. Chem Eng J 2012;195–196:91–102.
[33] McBride BJ, Zehe MJ, Gordon S. NASA Glenn coefficients for calculating thermodynamic properties of individual species. NASA, 2002 report TP-2002-21155; 2002.
[34] Laurendeau NM. Heterogeneous kinetics of coal char gasification and combustion. Prog Energy Combust Sci 1978;4:221–70.
[35] Menster M, Ergun S. Kinetics of oxygen exchange between CO_2 and CO on carbon. Carbon 1967;5:331–7.
[36] Essenhigh RH. Fundamentals of coal combustion. In: Elliot MA, editor. Chemistry of coal utilization, 2nd supplementary volume. New York: John Wiley and Sons; 1981. p. 1153–313.
[37] van Heek KH, Muhlen HJ. Chemical kinetics of carbon and char gasification. In: Lahaye J, Ehrburger P, editors. Fundamental issues in control of carbon gasification reactivity. Nato ASI series. Dordecht: Kluwer Academic Publishers; 1991. p. 1–34.
[38] Ergun SJ. Kinetics of the reaction of carbon dioxide with carbon. Phys Chem 1956;60:480–5.
[39] Hüttinger KJ. A method for the determination of active sites and true activation energies in carbon gasification: (1) theoretical treatment. Carbon 1990;28:453–6.
[40] Hüttinger KJ, Fritz OW. The carbon–carbon dioxide reaction: an extended treatment of the active-site concept. Carbon 1991;29:1113–8.
[41] Bhatia SK, Perlmutter DD. A random pore model for fluid–solid reactions: I. Isothermal, kinetic control. AIChE 1980;26:379–86.
[42] Young JB, Todd B. Modelling of multi-component gas flows in capillaries and porous solids. Int J Heat Mass Transfer 2005;48:5338–53.
[43] Lim JY, Dennis JS. Modeling reaction and diffusion in a spherical catalyst pellet using multicomponent flux models. Ind Eng Chem Res 2012;51:15901–11.
[44] Fuller EN, Schettler PD, Giddings JC. New method for prediction of binary gas-phase diffusion coefficients. Ind Eng Chem 1966;58:18–27.
[45] Cunningham RS, Geankoplis CJ. Diffusion in three-component gas mixtures in transition region between Knudsen and molecular diffusion. Ind Eng Chem Fundam 1968;7:429–32.
[46] Bohn CD, Cleeton JP, Müller CR, Davidson JF, Hayhurst AN, Scott SA, et al. The kinetics of the reduction of iron oxide by carbon monoxide mixed with carbon dioxide. AIChE J 2010;56(4):1016–29.
[47] Bohn CD, Müller CR, Cleeton JP, Hayhurst AN, Davidson JF, Scott SA, et al. Production of very pure hydrogen with simultaneous capture of carbon dioxide using the redox reactions of iron oxides in packed beds. Ind Eng Chem Res 2008;47:7623–30.
[48] Kidambi PR, Cleeton JPE, Scott SA, Dennis JS, Both CD. The interaction of iron oxide with alumina in a composite oxygen carrier during the production of hydrogen by chemical looping. Energy Fuels 2012;26:603–17.
[49] Wen CY, Yu YH. A generalized method for predicting minimum fluidization velocity. AIChE J 1966;12:610–2.
[50] Dennis JS, Lambert RJ, Milne AJ, Scott SA, Hayhurst AN. The kinetics of combustion of chars derived from sewage sludge. Fuel 2005;84:117–26.
[51] Darton RC, La Nauze RD, Davidson JF, Harrison D. Bubble growth due to coalescence in fluidized beds. Trans Inst Chem Eng 1977;55:274–80.
[52] Grabke HJ. Oxygen transfer and carbon gasification in the reaction of different carbons with CO_2. Carbon 1972;10:587–99.
[53] Bhatia SK, Perlmutter DD. A random pore model for fluid–solid reactions: II. Diffusion and transport effects. AIChE J 1981;27:247–54.
[54] Wang CT, Smith JM. Tortuosity factors for diffusion in catalyst pellets. AIChE J 1983;29:132–6.
[55] Kaza KR, Jackson R. Diffusion and reaction of multicomponent gas mixtures in isothermal porous catalysts. Chem Eng Sci 1980;35(5):1179–87.
[56] Hayhurst AN, Parmar MS. Measurement of the mass transfer coefficient and Sherwood number for carbon spheres burning in a bubbling fluidized bed. Combust Flame 2002;130:361–75.